Geosci. Model Dev. Discuss., 8, 6987–7061, 2015
www.geosci-model-dev-discuss.net/8/6987/2015/
doi:10.5194/gmdd-8-6987-2015

Geoscientific Model Development Discussions
Open Access

Towards convection-resolving, global atmospheric simulations with the Model for Prediction Across Scales (MPAS): an extreme scaling experiment

D. Heinzeller[1], M. G. Duda[2], and H. Kunstmann[1,3]

[1]Karlsruhe Institute of Technology, Institute of Meteorology and Climate Research, Kreuzeckbahnstr. 19, 82467 Garmisch-Partenkirchen, Germany
[2]National Center for Atmospheric Research, Mesoscale and Microscale Meteorology Laboratory, 3090 Center Green Drive, Boulder, CO 80301, USA
[3]University of Augsburg, Institute of Geography, Alter Postweg 118, 86159 Augsburg, Germany

Received: 24 July 2015 – Accepted: 6 August 2015 – Published: 26 August 2015

Correspondence to: D. Heinzeller (heinzeller@kit.edu)

Published by Copernicus Publications on behalf of the European Geosciences Union.

Abstract

The Model for Prediction Across Scales (MPAS) is a novel set of earth-system simulation components and consists of an atmospheric model, an ocean model and a land-ice model. Its distinct features are the use of unstructured Voronoi meshes and C-grid discretisation to address shortcomings of global models on regular grids and of limited area models nested in a forcing data set, with respect to parallel scalability, numerical accuracy and physical consistency. This makes MPAS a promising tool for conducting climate-related impact studies of, for example, land use changes in a consistent approach.

Here, we present an in-depth evaluation of MPAS with regards to technical aspects of performing model runs and scalability for three medium-size meshes on four different High Performance Computing sites with different architectures and compilers. We uncover model limitations and identify new aspects for the model optimisation that are introduced by the use of unstructured Voronoi meshes. We further demonstrate the model performance of MPAS in terms of its capability to reproduce the dynamics of the West African Monsoon and its associated precipitation. Comparing 11 month runs for two meshes with observations and a Weather Research & Forecasting tool (WRF) reference model, we show that MPAS can reproduce the atmospheric dynamics on global and local scales, but that further optimisation is required to address a precipitation excess for this region.

Finally, we conduct extreme scaling tests on a global 3 km mesh with more than 65 million horizontal grid cells on up to half a million cores. We discuss necessary modifications of the model code to improve its parallel performance in general and specific to the HPC environment. We confirm good scaling (70 % parallel efficiency or better) of the MPAS model and provide numbers on the computational requirements for experiments with the 3 km mesh. In doing so, we show that global, convection-resolving atmospheric simulations with MPAS are within reach of current and next generations of high-end computing facilities.

1 Introduction

The weather- and climate-modelling community is currently seeing a shift in paradigm from limited area models towards novel approaches involving global, complex and irregular meshes. Yet, regional models are commonly used in numerical weather prediction and to study past, current and future climate at high spatial and temporal resolution over areas of specific interest. A wealth of such models exists nowadays, which differ in their discretisation of the computational grid, their implementation of the numerical solvers, their parameterisation of physical processes, and most notably in their simulation results (e.g., Smiatek et al., 2009; Nikulin et al., 2012). Despite these differences, they share the common principle of nested modelling: Regional climate information is generated by supplying a set of initial conditions as well as time-varying lateral boundary conditions (LBCs; large-scale atmospheric fields such as wind, temperature, geopotential height and hydrometeors) and lower boundary conditions (sea-surface temperature, sea ice) to the regional model. The idea behind this approach is that the LBCs keep the regional climate model (RCM) solution consistent with the forcing atmospheric circulation, while small-scale patterns are generated with higher accuracy due to the increase in temporal and spatial resolution. Sub-grid scale processes in the RCM are included through parameterisations, which can be entirely different from those of the forcing global circulation model (GCM).

Supplying lateral boundary conditions to nested models can cause severe problems, up to the point where the RCM solution becomes inconsistent with the forcing data (Davies, 1983; Warner et al., 1997; Harris and Durran, 2010; Park et al., 2014). Starting off as an initial-value problem, the RCM solution gradually becomes a boundary value problem, which from a mathematical point of view represents a fundamentally ill-posed boundary value problem (Staniforth, 1997; Laprise, 2003). This is less of an issue in the context of numerical weather prediction (NWP), where typical model runtimes are 3 to 15 days, than in seasonal forecasting (weeks to months) and in regional climate modelling (years to centuries).

GMDD
8, 6987–7061, 2015

Title Page
Abstract Introduction
Conclusions References
Tables Figures
◀ ▶
Back Close
Full Screen / Esc
Printer-friendly Version
Interactive Discussion

A common problem for both short- and long-term forecasting is that the solution of the RCM seems to vary with the size of the computational domain, as well as location and season (Caya and Biner, 2004; Leduc and Laprise, 2008; Caron, 2013). Several authors have shown that nudging techniques (grid or spectral nudging) towards the large-scale features of the forcing model can reduce these adverse effects, but that they can also hide model biases (von Storch et al., 2000; Miguez-Macho et al., 2004).

Further, the technique of grid nesting introduces discontinuities in spatial resolution between the regional model and the coarser-grid driving model, as well as between the nests within the regional model itself. For a typical refinement ratio of 3, two-thirds of the spatial wave-number spectrum present in the fine mesh are absent in the coarse mesh (Park et al., 2014). This implies that (a) these features must be spun up for inflows into the higher-resolution domain, and that (b) these wave numbers are reflected at the domain boundary for outflows from the high-resolution domain to the coarser domain. To address the latter issue, filters that are efficient over a large range of wave numbers are required. The temporal interpolation required by nesting can introduce further numerical artefacts, in particular when interpolating forcing LBCs, usually available at 3–6 h timesteps, to the model integration time step of the high-resolution domain (typically 6 s per 1 km grid size).

One obvious solution is to avoid using LBCs and nesting by running a global model at the resolution required for the area of interest. This, however, is prohibitively expensive or simply not feasible, even on the latest generations of supercomputers. An intermediate approach therefore is to run a global model at a moderate resolution and use a smooth mesh transition on a variable-resolution grid, where filters are efficient at the local scale of the corresponding grid cell (Ringler et al., 2011). Beside the here-discussed MPAS model, few other recent developments such as ICON (ICOsahedral Non-hydrostatic model, Zaengel et al., 2015), adopt this strategy. Applying such models for mid- and long-term regional climate simulations has only recently become possible and requires substantial computational power.

GMDD
8, 6987–7061, 2015

The Model for Prediction Across Scales (MPAS)[1] is a recent numerical modelling framework that includes an atmospheric model MPAS-A (Skamarock et al., 2012), an ocean model MPAS-O (Ringler et al., 2013), and a land-ice model MPAS-LI. The MPAS model is a collaborative project, led by the National Center for Atmospheric Research (NCAR) and the Los Alamos National Laboratory (LANL). The three components of MPAS in principle form a so-called Earth System Model (ESM), but a coupler between them is not yet available. A common feature of the three MPAS constituents are unstructured, centroidal Voronoi meshes (spherical centroidal Voronoi tessellations, SCVTs Du et al., 2003), which allow the generation of global, irregular, variable-resolution meshes with smooth transitions between areas of different refinement.

The atmospheric model MPAS-Atmosphere is a global, fully-compressible non-hydrostatic model using finite-volume numerics. Based on the Voronoi mesh, the model uses a C-grid staggering for the state variables (i. e., wind components are modelled at the faces of every cell, and the prognosed component of the wind is orthogonal to the cell face) as described in Thuburn et al. (2009) and Ringler et al. (2010). The governing equations can then be cast in a way such that energy, momentum and water vapour content are conserved. The MPAS-A model builds on existing, well-established techniques of the Advanced Research Weather Research and Forecasting model (WRF-ARW, Skamarock et al., 2008), for example the split-explicit time integration scheme for the solution of the horizontal advection. It also contains a subset of WRF's physics parameterisations that are suitable for climate modelling purposes. While WRF uses a terrain-following hydrostatic pressure coordinate for the vertical discretisation, MPAS employs a height-based terrain-following vertical coordinate. The latter discretisation reduces artificial circulations caused by inaccuracies in the horizontal pressure gradient term (Klemp, 2011).

Until recently, advances in computational power following Moore's Law were mainly driven by transistor speed and energy scaling, as well as by micro-architecture ad-

[1]http://mpas-dev.github.io

vances. Physical limitations and practical energy concerns will create new challenges for continued performance scaling in the coming decades. In consequence, large-scale parallelism and the use of accelerators will be required to achieve performance and energy efficiency (Borkar and Chien, 2011). Hence, a key aspect of modern numerical codes is their ability to scale on massively parallel systems. The quasi-uniform centroidal Voronoi meshes used by MPAS are similar to icosahedral (hexagonal) meshes and can provide nearly uniform resolution over the globe, as opposed to latitude–longitude grids that require polar filtering to overcome the issue of converging grid lines at the poles. Grids requiring polar filtering or spherical transform methods do not scale very well on massively parallel systems (Skamarock et al., 2012). With MPAS, an efficient parallelisation can be achieved by aligning all grid cells in a 1-D array, with the vertical coordinate stacked on top as the second dimension (MacDonald et al., 2011). Good scaling has been achieved in early weak and strong scaling tests. However, a thorough investigation of the scalability of MPAS on parallel and massively parallel systems has not yet been conducted.

In this study, we investigate the performance of MPAS for different problem sizes on four HPC facilities in Europe. For each problem, strong scaling tests are conducted on all four platforms, which cover a range of different architectures to reflect the large variety of computational systems available for research. Additionally, we conduct extreme scaling tests using a 3 km global mesh to study the scalability of MPAS up to nearly half a million tasks and to demonstrate that global, convection-resolving simulations are becoming possible. We explore the limits of the MPAS model when its parallel efficiency breaks down and identify opportunities for improvement. We further derive estimates on the feasibility to conduct longer runs at convection-resolving resolution on current HPC facilities.

We also assess the quality of the MPAS model output in terms of its accuracy for climate modelling. We have chosen to study the particular problem of reproducing the characteristics of the West African Monsoon (WAM). The WAM is the most prominent feature of the West African climate and accounts for the majority of the annual precipitation. Differential heating of the ocean and the land surface cause a seasonal change of the large-scale wind systems during boreal summer, which results in the migration of the inter-tropical convergence zone (ITCZ) and the associated rain band northwards over the West African continent. The WAM is driven by a complex and not yet fully understood interplay of various dynamical features (e.g., Sultan et al., 2003; Grist and Nicholson, 2001; Nicholson and Webster, 2007). Global circulation models (GCMs) often fail to reproduce this annual movement of the ITCZ due to their limited temporal and spatial resolution (e.g., Hourdin et al., 2010; Sylla et al., 2010). Despite their deficiencies discussed above, regional climate models can improve the representation of precipitation in comparison to their forcing data set (Nikulin et al., 2012; Klein et al., 2015). Variable-resolution meshes permit resolving the region of interest (greater West Africa in this case) at high resolution, while keeping the model aligned with large-scale features outside of this area. It is hoped that this will lead to an improvement of the representation of the WAM. It also opens up the possibility to study processes such as the teleconnection between the Indian Monsoon and the West African Monsoon (Rodwell and Hoskins, 1996), or the impact of land use changes on weather and climate in a consistent approach.

The paper is organised as follows: in Sect. 2, we introduce the HPC facilities used for this study, provide details about the MPAS-A code, and present the scaling experiments with moderate problem sizes. We continue in Sect. 3 with an analysis of the physical accuracy of the MPAS model in comparison to observational data and data from own regional climate modelling experiments. Section 4 is devoted to the extreme scaling tests, and Sect. 5 summarises our findings and gives an outlook on future modelling activities.

2 Scaling experiments for moderate problem sizes

We perform strong scaling experiments for three different meshes and on four HPC facilities in Europe. The problem sizes range from a regular 120 km mesh with 40 962 cells as the smallest problem to a large, variable-resolution 60–12 km mesh with 535 554 grid cells. An intermediate test case with a variable-resolution 100–25 km mesh with 163 842 grid cells is studied as well.

2.1 HPC facilities

Two of the four HPC systems, the Très Grand Centre de Calcul (TGCC) Curie[2] and the Forschungszentrum Jülich (FZJ) Juqueen[3], belong to the largest machines in Europe and are part of the PRACE Tier-0 pool[4]. They are based on entirely different architectures, with Curie being a Bull Linux-cluster type system using Intel Sandy Bridge CPUs, and Juqueen an IBM Bluegene/Q. The third system, the Steinbruch Centre for Computing (SCC) ForHLR1[5], went into operation in September 2014 and is based on the Intel Ivy Bridge architecture. Lastly, the FZJ Juropatest[6] is a cutting-edge prototype system incorporating Intel Haswell CPUs, and a pilot for the future FZJ Jureca (successor of FZJ Juropa) system.

2.1.1 TGCC Curie

The TGCC Curie consists of 360 "fat nodes" and 16 "hybrid nodes", not used in this study, and 5040 "thin nodes" of type B510 Bullx, with 2 eight-core Intel processors Sandy Bridge EP (E5-2680) at 2.7 GHz, 64 GB RAM, and a local SSD disk each. An InfiniBand QDR Full Fat Tree network is used for both the compute network and the I/O to the global LUSTRE file system with 5 PB capacity (100 GB s^{-1} storage bandwidth).

[2] http://www-hpc.cea.fr/en/complexe/tgcc-curie.htm

[3] http://www.fz-juelich.de/ias/jsc/EN/Expertise/Supercomputers/JUQUEEN/JUQUEEN_node.html

[4] http://www.prace-ri.eu/prace-resources

[5] http://www.scc.kit.edu/dienste/forhlr.php

[6] http://www.fz-juelich.de/ias/jsc/EN/Expertise/Supercomputers/JUROPATEST/JUROPATEST_node.html

GMDD
8, 6987–7061, 2015

The machine went into service in 2012, and since then two further generations of Intel CPUs were launched (Intel Ivy Bridge, Intel Haswell). With 3 different node types, Curie addresses a wide range of scientific challenges and offers an aggregate peak performance of 2 Petaflops. We use the Intel compilers icc/ifort and the Bullmpi MPI library to compile MPAS on Curie (see below for details).

2.1.2 FZJ Juqueen

The FZJ Juqueen is an IBM Bluegene/Q system and was installed in 2012/13. It hosts 28 racks with 1024 nodes per rack and 16 cores per node, which totals to 458 752 physical cores. Simultaneous multi-threading (SMT) with 2 or 4 threads per core is supported by the hardware, but not used in this study due to the lack of threading in MPAS-A (see below). Each node consists of 16 IBM PowerPC A2 cores with 1.6 GHz, and hosts 16 GB RAM. A 5-D Torus interconnect with 40 $GB\,s^{-1}$ is used as compute network, while I/O is redirected to dedicated I/O nodes (typically 8 per rack) using a 10 Gb Ethernet to connect to the GPFS file system (200 $GB\,s^{-1}$ bandwidth). The peak performance was measured as 5.9 Petaflops (Linpack: 5.0 Petaflops). With a large number of relatively slow CPUs and a small memory per core, Juqueen most resembles the future massively parallel systems described above. As such, porting and scaling experiments of numerical codes onto this architecture are as challenging as instructive for future applications. The thread-safe version of the IBM XL compilers bgxlc_r/bgxlf95_r and their respective MPI wrappers are used to compile MPAS on Juqueen.

2.1.3 SCC ForHLR1

The ForHLR1 is the most recent addition to the SCCs high performance computing systems and is the first of two stages in the expansion of the parallel computing facilities at SCC. Like Curie, it hosts different types of nodes to cater for the various needs of the modelling community: the workhorse for parallel applications, and used in this study, are 512 “thin nodes” with 2 ten-core Intel Ivy Bridge processors (E5-2670v2) at 2.4 GHz and 64 GB RAM, connected via an Infiniband FDR interconnect. The theoretical peak performance of these 512 nodes is 216 Teraflops. A central LUSTRE filesystem is attached to the nodes, using the same Infiniband interconnect for I/O as for the compute network. We use the Intel compilers icc/ifort 14.04 and the corresponding Intel MPI library to compile MPAS.

2.1.4 FZJ Juropatest

The FZJ Juropatest cluster is a relatively small prototype system and consists of 60 T-Platform V210s blades with 2 fourteen-core Intel Haswell processors (E5-2695v3) at 2.3 GHz and 128 GB RAM each. The compute network is an Infiniband FDR with non-blocking Fat Tree topology, while I/O to the central GPFS file system is realised via 10 Gb Ethernet. With a peak performance of 72 Teraflops, Juropatest allows users of JSC's current general purpose supercomputer Juropa to port and optimise their applications for the new Haswell CPU architecture. While optimising the MPAS model for the Haswell features and instruction sets is beyond the scope of this study, it will become an inevitable step in future model development and tuning. We use the available Intel Compilers, here icc/ifort 2015.1.133, and the corresponding Intel MPI library to compile MPAS. On Juropatest, we conduct two sets of runs for each of the test cases: for the first set (*Jtest-half* in the following), we use only one of the two available fourteen-core CPUs in each node, which implies a similar number of cores per node for Curie and Juropatest or, in other words, a similar number of nodes for the same total number of tasks. In this configuration, each task is bound to one core on the node. For the second set (*Jtest-full* in the following), we use both CPUs, i. e., 28 cores on each node to exploit the capabilities of the Juropatest system and possible memory bandwidth limitations of MPAS-A.

GMDD
8, 6987–7061, 2015

2.2 MPAS-A code

For the strong-scaling studies in this paper, we use MPAS-A v3.1, released on 24 November 2014. This release of the model employs a horizontal domain decomposition for parallel execution, and parallelisation is implemented using MPI only; in this version of the code, no threading is used. The MPAS code is written almost entirely in Fortran 2003, with a few minor parts written in C. The MPAS build system uses only the `make` utility, with settings for different compilers and architectures described as different targets in the top-level `Makefile`; see Appendix A for the compiler flags used in this study.

The optimal parallelisation and distribution of the cells of the Voronoi mesh for a given number of tasks is treated as a graph partitioning problem. The dual mesh of a Voronoi tessellation is a Delaunay triangulation, which immediately provides the connectivity graph for the primal (i. e., Voronoi) cells in the mesh. In MPAS, the graph partitioning is computed as a separate pre-processing step, for which the METIS software is used[7]. An optimal partitioning distributes equal work (by proxy, the number of cells) to each task while minimising the edge cut (assumed to model the communication between tasks). METIS uses a multilevel k-way partitioning scheme, which produces partitions of comparable quality to traditional multilevel bisection algorithms and is about two orders of magnitude faster (Karypis and Kumar, 1998). The resulting graph partitioning can be critical for the model performance due to, for example, a large overhead of communication and computational imbalances between the individual partitions.

At start-up, the MPAS-A model reads a file that assigns Voronoi cells to each of the MPI tasks according to a partitioning produced by METIS. The set of cells assigned to an MPI task is referred to as a “block”, and the cells in this assignment are referred to as the “owned” cells. The dynamical solver in MPAS-A requires stencils of cells in order to apply various operators, and as part of the model start-up, referred to internally as the “bootstrapping” process, a pre-determined number of layers of halo cells (some-

[7]http://glaros.dtc.umn.edu/gkhome/views/metis

GMDD
8, 6987–7061, 2015

times referred to as "ghost" cells in other modeling systems) are added around each block. Although the number of halo cells can vary between different MPAS models, as illustrated in Fig. 2, MPAS-A adds two layers of halo cells around each block of cells. At points in the MPAS-A dynamical solver where current values of fields in halo cells are required, values are communicated between tasks, from owned cells to ghost cells, with point-to-point MPI communications.

An important aspect and common bottleneck in numerical weather prediction and climate modelling is disk I/O, since large 4-D fields such as temperature, geopotential height, or wind components need to be written to disk frequently. In MPAS v3.1, I/O is facilitated by the parallel I/O library PIO v1.7.1, a wrapper with an easy-to-use API that encapsulates the complexity of parallel I/O for a number of supported formats: binary, serial NetCDF[8], Parallel-NetCDF[9], and recently (since v.1.9.14) parallel NetCDF-4 through PHDF5[10] (Dennis et al., 2013). PIO is compiled without further optimisation (standard settings) on all four machines. The HDF5, NetCDF and Parallel-NetCDF libraries are provided as modules on all four systems.

Unless stated otherwise, all experiments are conducted with double precision floating point precision, 41 atmospheric levels, 4 soil levels, a full suite of physics and dynamics (see Appendix B for details), and standard disk I/O. Each experiment is run for 24 h model time, during which an initial conditions file is read (`init.nc`), diagnostic output files are written every 3 h (`diag.nc`), and a final restart file and a comprehensive output file are written at the end (`restart.nc`, `output.nc`). The model integration time step depends on the grid resolution and is mentioned in the individual sections below. Note that for variable resolution meshes, the global time step is determined by the smallest grid size. By default, all tasks participate in the parallel I/O.

[8]http://www.unidata.ucar.edu/software/netcdf

[9]http://trac.mcs.anl.gov/projects/parallel-netcdf

[10]http://www.hdfgroup.org/HDF5

GMDD
8, 6987–7061, 2015

2.3 Regular 120 km grid

The first and smallest test case consists of a global, regular 120 km mesh with 40 962 grid cells, which is roughly comparable in resolution to a 284 × 142 latitude–longitude grid. It is thus in the range of current earth system models. A model integration time step of 150 s is adopted. For a resolution of 120 km, this is an extremely conservative setting (1.25 s per km grid size) for MPAS-A, which implies 576 integration time steps for a 24 h test run, compared to 120–144 integration time steps for typical values of 5–6 s per km grid size. This increases the time spent for the actual parallel integration relative to that for model initialisation and disk I/O. The 120 km grid is illustrated in Fig. 3, while Fig. 4 shows the scaling plots on the four HPC facilities described above. For an easier comparison of the scalability of the different test cases, the scaling is displayed as parallel efficiency (i. e., the ratio of real scaling and ideal scaling) vs. the number of tasks (bottom horizontal axis) and number of cells owned per task (top horizontal axis). Table D1 provides further details about the scaling, whereas Table G1 summarises the size of the files to be read and written during one model run.

Previous scaling tests on NCAR's Yellowstone supercomputer[11] suggest that for regular meshes, the parallel efficiency of MPAS-A is correlated with the number of cells owned per task. Considering the time required for the solver only, i. e., neglecting the setup costs and the disk I/O, a parallel efficiency of close to 70 % is obtained for more than 160 cells per task. Here, we include the setup costs (bootstrapping and reading of initial conditions file) and the output to disk in the scaling to emphasise the importance of all aspects of the system – from filesystem performance to compute performance to the speed of the interconnect – and to estimate the necessary resource requirements. It should be noted that this can have a negative and noticeable influence on the parallel efficiency, depending on the performance of the parallel I/O operations and the ratio of the time spent for the setup of the model and the actual time integration. Hence, the threshold of 160 cells owned per task for the breakdown of the parallel efficiency should

[11] https://www2.cisl.ucar.edu/resources/yellowstone

GMDD
8, 6987–7061, 2015

be considered as a lower limit. In Sect. 2.6, we provide a detailed analysis of the costs of the individual steps for the Jtest-full system.

On the three Linux-cluster type systems, test runs are conducted on single nodes up to 32 (Curie), 20 (ForHLR1), 15 (Jtest-full) and 30 (Jtest-half) nodes. In the following, we refer to "good scaling" as a parallel efficiency of $\approx 70\,\%$ or more. Good scaling is achieved up to 6 nodes on Curie (96 tasks, or 427 grid cells per task), 9 nodes on ForHLR1 (180 tasks, or 230 grid cells per task), 8 nodes on Jtest-full (224 tasks, or 183 grid cells per task), and 15 nodes on Jtest-half (210 tasks, or 190 grid cells per task). Comparing Curie and Jtest-half, it is evident that a single Haswell CPU with 14 cores outperforms two Sandy Bridge CPUs with 2×8 cores on the same board, and that (b) the parallel efficiency decreases faster with the number of nodes on Curie. This is probably related to the interconnect: while Juropatest (as well as Yellowstone) uses Infiniband FDR Full Fat Tree technology (Fourteen Data Rate, theoretical effective throughput $14\,\mathrm{Gb\,s^{-1}}$ per connection) for the inter-process communication (MPI) and a separate 10 Gb Ethernet connection for I/O operations, Curie uses QDR Full Fat Tree technology (Quad Data Rate, theoretical effective throughput $4\,\mathrm{Gb\,s^{-1}}$ per connection) for the inter-process communication *and* for I/O operations. The transition zone for the breakdown of the parallel efficiency is indicated as shaded blue area in Fig. 4. A comparison of the absolute runtimes on Jtest-half and Jtest-full shows that runs with 28 cores per node are 5–15 % slower than runs with 14 cores per node, which is presumably due to memory bandwidth bottlenecks.

The minimum job (and block) size on Juqueen is 32 nodes or 512 tasks, which corresponds to only around 80 cells owned by each task. The parallel efficiency drops rapidly with increasing number of nodes, since this problem size is simply too small for application on Juqueen. Figures 8 and 9, left panels, display the communication volume and the number of non-contiguous partitions (number of tasks with spatially disconnected patches) of the partitions as function of the number of tasks. While the communication volume scales linearly with the number of tasks up to about 1000 tasks (approx. 40 owned cells per task), the relationship becomes non-linear for larger numbers of tasks.

Title Page
Abstract Introduction
Conclusions References
Tables Figures
◀ ▶
Back Close
Full Screen / Esc
Printer-friendly Version
Interactive Discussion

At the same time, the graph partitions become increasingly non-contiguous. It should be noted that the values displayed in Figs. 8 and 9 are computed by METIS and as such are a function of the partitioning of the cells only, which essentially assumes a single layer of ghost cells. Since MPAS-A exchanges two layers of ghost cells at maximum, the actual number of ghost cells, edges and vertices can be slightly different. A detailed study of the impact of these graph properties will be given in the following section.

Table G2 lists the cheapest model runs in terms of CPUh spent per 24 h model integration and the fastest runs in terms of realtime per 24 h model integration for the four HPC sites. It is important to remember that while the Jtest-half runs use only 50 % of the available cores on each node, the computational costs for the full node (28 CPUh per node per hour real time) are charged for the model run, since the node is not available for other users or jobs. Also, a one-to-one relation of CPUh between Linux cluster-type machines and an IBM Bluegene is not meaningful. By comparing typical calls for proposals for the different HPC systems, a conversion factor of 1 : 16 seems to be reasonable, i. e., to consider one entire node with 16 cores on Juqueen as equivalent to one core on the other systems. However, since applications for computing resources usually demand estimates for the required amount of CPUh, we list the actual CPUh here.

2.4 Variable 100–25 km grid

The second test case employs an irregular mesh with a variable resolution ranging from 100 km for most parts of the globe to 25 km for a circular area spanning about 60°, and centred on West Africa (lat = 12.5° N, lon = 0° E). An integration time step of 120 s is used. The mesh as well as the frequency distribution of cell sizes are displayed in Fig. 5, the scaling is illustrated in Fig. 6 and summarised in Table E1.

Tests runs are conducted on single nodes up to 192 nodes on Curie (3072 tasks, 53 owned cells per task), 60 nodes on ForHLR1 (1200 tasks, 137 owned cells per task), 35 nodes on Jtest-full (980 tasks, 167 owned cells per task), and 60 nodes on Jtest-half (840 tasks, 195 owned cells per task). Good scaling is achieved up to 32 nodes

GMDD
8, 6987–7061, 2015

on Curie (512 tasks, 320 owned cells per task), 20 nodes on ForHLR1 (400 tasks, 410 owned cells per task), 25 nodes on Jtest-full (700 tasks, 234 owned cells per task), and 35 nodes on Jtest-half (490 tasks, 334 owned cells per task). The parallel efficiency on average drops from about 90 to 40 % within the transition zone (shaded area in Fig. 6, 600 to 150 cells owned per task), similar to the first test case on the regular 120 km mesh.

Notably different to the previous test case are the measured runtimes for Jtest-full and Jtest-half: for small numbers of tasks, the Jtest-full runs show a worse performance due to the aforementioned memory bandwidth limitations. For large numbers of tasks (nodes), the increase in inter-node MPI communication, which impacts the Jtest-half runs more than the Jtest-full runs, becomes the limiting factor and decreases the performance of the Jtest-half runs below that of the Jtest-full runs. With respect to the remaining HPC systems, a clear separation of the parallel efficiency by interconnect technology as for the 120 km test case cannot be seen here, due to the following reasons:

Firstly, the disk I/O demand scales with the number of grid cells and is larger by a factor of 4 for this mesh (see Table G1). As we will see in the following sections, in particular for the extreme scaling experiments in Sect. 4, the disk I/O becomes increasingly important for larger problem sizes and can consume a significant part of the total runtime. The I/O is routed differently at the four HPC sites, the central storage systems have different bandwidths and block sizes, and the parallel I/O libraries might perform differently, depending on the compilers and compilation flags. Additionally, in this test case we adopt an integration time step of 120 s (4.8 s per km grid size), which implies a smaller fraction of the total time spent for the actual time integration relative to the disk I/O.

Secondly, the graph partitioning adds another layer of complexity and variability to the performance diagnostics. Figures 8 and 9 display key properties of the graph partitions for the three test cases. The above-mentioned linear relationship between the communication volume and the number of tasks also holds for the variable 100–25 km mesh up to about 40 owned cells per task (4000 tasks). Different from the regular 120 km mesh, the number of non-contiguous partitions does not follow a clear pattern: for more than 40 owned cells per task, Fig. 9 suggests that METIS by default tends to create more non-contiguous partitions for complex mesh structures, and that this occurs predominantly for numbers of partitions which are not powers of 2. Both graph partitioning algorithms implemented in METIS, recursive bisectioning and direct k-way partitioning, are naturally embedded in the binary system and it therefore seems to be reasonable that METIS favours partitioning into number of patches that are powers of 2.

This variability introduced by the graph partitioning is unpredictable and may have significant impact on the model performance. If not instructed otherwise, the graph partitioning tool METIS aims at minimising the edge cut (communication volume), which potentially comes at the cost of having non-contiguous partitions. As discussed earlier in Sect. 2.2, halo cells are added around each patch of the individual tasks, for which communication with the neighbouring tasks is required. The additional amount of communication caused by halo cells around non-contiguous partitions can be substantial, in particular if the number of cells owned per task is small (i. e., the ratio of halo cells to owned cells is large).

To investigate the effect of non-contiguous partitions on the parallel efficiency, we analyse one partition with 300 tasks for the 100–25 km mesh on ForHLR1 (546 owned cells per task), for which METIS by default produces a non-contiguous partition. We create an additional, contiguous partition using the command line arguments `-contig -minconn` for METIS, which results in an increase of the edge cut from 58 031 to 58 870 (1.4 %). Figure 7 displays the total number of cells (nCellsByTask), the number of owned cells (nCellsSolveByTask), and the number of halo cells per task (nHaloCellsByTask) as ratio between the non-contiguous and the contiguous partition. Since the communication volume increases for the contiguous partition, the total number of cells per task on average is larger, too. The average number of owned cells is identical, since the number of cells of the graph does not change. Notably, task 200 has a 1.3 times

GMDD
8, 6987–7061, 2015

larger number of halo cells for the non-contiguous partition, since its partition consists of two separate patches, which implies a larger number of neighbouring tasks and of surrounding halo cells. To eliminate the influence of the disk I/O on the runtimes for the two partitions, we switch off the output to disk. We find that the measured runtimes for the model integration is practically identical for the two runs (251 s non-contiguous vs. 255 s contiguous). For 300 tasks, the average ratio of halo cells to owned cells is 1 : 2.8, which might be too small to see the effect of the additional halo cells in the non-contiguous partition. We therefore repeat the test for non-contiguous and contiguous partitions for 2520 tasks (65 owned cells per task), with a corresponding ratio of 1.2 : 1 halo cells to owned cells. Even in this case, the measured runtimes for the model integration are nearly identical (45.2 s contiguous vs. 45.6 s non-contiguous). We conclude therefore that the impact of non-contiguous partitions on the runtime is negligible for any reasonable number of tasks for a given mesh.

Although the number of grid cells is 4 times larger for this test case than for the regular 120 km mesh, the problem size is still too small for application on Juqueen. The two smallest possible parallel runs with 512 and 1024 tasks correspond to 320 and 160 cells owned per task, for which the decrease in parallel efficiency is 20 %. Runs with larger number of tasks all have parallel efficiencies of less than 60 %. Table G2 lists the cheapest and fastest model runs for the four HPC sites.

2.5 Variable 60–12 km grid

The third moderately-sized scaling test consists of a variable resolution mesh with maximum grid spacing 60 km and minimum grid spacing of 12 km. The refinement area is an approximate ellipse, illustrated in Fig. 10, and encompasses the whole of North and Central Africa, extends as far as India in the East and covers a large part of the Atlantic Ocean in the West. This particular mesh is useful for studying the teleconnection between the Indian and Atlantic Ocean and the monsoon systems in East and West Africa. The total number of grid cells is 535 554, which corresponds to 1034 × 517 grid points on a regular latitude–longitude grid and thus is in the range of current reanalyses. A time step of 72 s (6 per km grid size) is adopted.

Figure 11 and Table F1 summarise the scaling of this mesh on the four systems. As for the variable 100–25 km mesh, a separation of the parallel performance by interconnect cannot be detected, due to the increasing variability introduced by the disk I/O (see Table G1) and the layout of the graph partitions (Figs. 8 and 9, right panels). While the number of tasks is sufficiently large to obtain a linear relationship between the communication volume and the number of tasks up to 16 384 tasks on Juqueen, the complexity of the mesh leads to more non-contiguous partitions, in particular on ForHLR1 and Juropatest, where the number of tasks are multiples of 20 and 14. For Curie, all partitions are contiguous even without the use of the `-contig` option in METIS.

Tests runs are conducted on single nodes up to 384 nodes on Curie (6144 tasks, 87 owned cells per task), 100 nodes on ForHLR1 (2000 tasks, 268 owned cells per task), 55 nodes on Jtest-full (1540 tasks, 348 owned cells per task), and 55 nodes on Jtest-half (770 tasks, 696 owned cells per task). Good scaling is achieved up to 56 nodes on Curie (896 tasks, 598 owned cells per task), 45 nodes on ForHLR1 (900 tasks, 595 owned cells per task), and up to the maximum number of 55 nodes on Jtest-full and Jtest-half. In the transition zone between 600 and 150 owned cells per task, shaded in blue, the parallel efficiency on Curie and ForHLR1 drops off quickly from about 75 % to as low as 30 %.

Juropatest shows the best, but most irregular scaling of the three Linux-cluster systems, a consequence of the variability of the disk I/O and of the mesh partitioning. With a maximum of 55 available nodes on the system, the parallel performance is better than 70 % for both Jtest-half and Jtest-full. The parallel efficiencies for ForHLR1 and Curie follow a more regular trend, although the number of non-contiguous partitions is highly variable for ForHLR1, but not for Curie. This adds further support to our conclusion that the impact of non-contiguous partitions on the runtime is negligible for any reasonable number of tasks for a given mesh. With 535 554 grid cells, this test case

GMDD
8, 6987–7061, 2015

also shows good scaling on Juqueen up to 128 nodes (2048 tasks, 262 owned cells per task). For larger number of tasks, the parallel efficiency drops rapidly and constantly and the number of non-contiguous partitions becomes highly variable.

We further address the question how the total runtimes compare on the various HPC systems. Due to the large differences in tasks between the Linux-cluster systems and the Bluegene system, the problem size must be large enough for a fair comparison. While this was not the case for the previous two test cases, the 60–12 km mesh allows such a comparison. Figure 12 displays the total runtimes for the 24 h model runs on the four systems. Firstly, the three Linux-type systems line up quite well, which means that the absolute runtimes are very close for similar parallel decompositions. For more than 1000 tasks (less than 600 owned cells per task), the realtime required for a 24 h model integration flattens out at about 530 s. An increase in runtime is expected for very large parallelisations on these systems (10 000 tasks or more). The runtimes on the Bluegene system Juqueen show the same pattern, but flatten out for more than 4000 tasks (less than 134 owned cells per task) at 2500 s, about 5 times slower than on the other systems. The shift in the breakdown of the parallel performance to larger parallelisations on Juqueen can be attributed to the 5-D Torus interconnect with a maximum bandwidth of 40 GB s^{-1}, 10 times more than Infiniband QDR on Curie and 3 times more than Infiniband FDR on ForHLR1 and Juropatest. For less than 4000 tasks, the runtimes on Juqueen are up to 10 times longer than on the Linux-cluster systems.

Table G2 lists the cheapest model runs in terms of CPUh spent per 24 h model integration and the fastest runs in terms of realtime per 24 h model integration for the four HPC sites.

2.6 Breakdown of parallel performance

In the following, we investigate the reasons for the breakdown of the parallel performance. In the previous scaling tests, we include the model setup – principally, bootstrapping and reading of the initial conditions file – as well as the parallel output to disk in the measurements. Here, we split up the total computational costs and the parallel performance into three different steps: time integration, model setup, and disk output. Over longer runs, the model initialisation costs are amortised and the parallel performance is determined by the numerical solver (time integration) and the parallel I/O (disk output). Accordingly, Fig. 13 displays the total computational costs, the costs for the three steps, and for a combination of time integration and disk output for the Jtest-full system and all test cases. Each time, the parallel efficiency of the time integration only is above-ideal for more than 600 owned cells per task ("left" of the transition zone, indicated as shaded area) and slowly decreasing within the transition zone (600–150 owned cells per task). The model setup and disk output, on the other hand, are only weakly dependent on the number of tasks and therefore their parallel efficiency drops rapidly. The parallel performance of longer runs than the 24 h tests conducted here is indicated with orange stars and drops from 100 % or more to about 80 % within the transition zone.

According to Fig. 13, the parallel performance of the dynamical solver is high down to 150 owned cells per task, but starts to decrease within the transition zone. To exploit the limiting factors of the solver for large number of tasks, we use the parallel debugging and profiling tools Scalasca[12] and Score-P[13]. These tools are available as modules on Juqueen, hence we focus on two particular runs on this system. We analyse in detail the 2048-task run on the 60–12 km mesh (261 owned cells per task) and the 1024-task run on the 100–25 km mesh (160 owned cells per task), which are both close to the lower limit of good scaling (70 % parallel efficiency).

As discussed previously, halo cells are added around each patch of the individual tasks, for which communication with the neighbouring tasks is required. The larger the number of tasks, the smaller the number of owned cells per tasks, and the larger the ratio between halo cells and owned cells. The piecharts in Fig. 14 illustrate the percentages of time spent in selected routines for both runs. The total time spent for communication (grey to black colours: exchange halo fields, bootstrapping (initial), all-

[12]http://www.scalasca.org

[13]http://www.vi-hps.org/projects/score-p

GMDD
8, 6987–7061, 2015

MPAS: an extreme scaling experiment

D. Heinzeller et al.

to-all min/max values) is 30–31 % for both runs. Since the bootstrapping is only required during model initialisation to set up the halo fields and exchange lists, it becomes less important in the context of longer runs. On Juqueen, these longer runs will use 23–24 % of the model integration time for MPI communication. A detailed analysis of the Scalasca report reveals that most of this time is "wasted" in `MPI_WAIT` during the exchange of 2-D and 3-D halo fields for the 1024-task run on the 100–25 km mesh, which accounts for 17 % of the total time spent for the 24 model run.

Another significant fraction of 24–25 % is spent for the parallel I/O (purple to violet colours: build/write output stream, boundary updates (read), reading initial conditions). Reading the initial conditions occurs only during model initialisation. Thus, longer runs will use 12 % (left panel, 100–25 km mesh) or 16 % (right panel, 60–12 km mesh) for parallel I/O during the model integration. While most of the percentages are similar for the two profiles, there is a noticeable difference in reading the boundary updates (purple, 1 % left panel vs. 5 % right panel). A closer look at the Scalasca report reveals that also computational imbalances in the parallelisation can have serious impacts. For the example of the 2048-task run on the 60–12 km mesh, the average time required to update the boundary information (sea-surface temperature, sea-ice fraction) is about 11.8 s per task. However, one single task takes 19.3 s for the same action and blocks all remaining tasks in their execution. Computational imbalances are also detected for the 1024-task run on the 100–25 km mesh, where the execution time for the short-wave radiation scheme is 3.6 s on average, but 19.2 s at maximum (corresponding to 1.6 % of the total execution time). Since the model synchronisation takes places when exchanging halo cell data, the different computing times of the model physics appear in the time spent for communication.

Subtracting the times required for MPI communication and for parallel I/O leaves approximately 45 % of the total time for the actual model integration. This highlights the importance of an efficient parallelisation and fast interconnects between the compute nodes and to the central storage, in particular for future applications on massively parallel systems and for the extreme scaling tests in Sect. 4.

GMDD
8, 6987–7061, 2015

MPAS: an extreme scaling experiment

D. Heinzeller et al.

3 Reproducing the dynamics of the West African Monsoon

The second important aspect of a numerical weather prediction and climate model is its accuracy in reproducing observed meteorological conditions on global, regional and local level. As described in the introduction, the West African Monsoon has turned out to be a notoriously difficult problem in climate modelling, since it is a complex interplay of various dynamical, microphysical and surface-related processes across scales. The common understanding is that the intensity of the monsoon and the associated precipitation on local scales are regulated by the driving, large-scale atmospheric circulation. This picture is challenged and complicated by a recent study of Klein et al. (2015), who found that processes on local scale such as mesoscale convection and precipitation events, can have a noticeable influence through feedback effects on the entire monsoon system. Examples therefore are enhanced moisture transport and circulation, and strengthening of westward traveling disturbances (African Easterly Waves).

In this study, we attempt a first and brief evaluation of the ability of MPAS-A to reproduce the dynamics of the West African Monsoon. Due to computational limitations for this short comparison, we are restricted to 11 month long model runs. We focus on the onset of the monsoon season in June/July 1982 for two of the meshes presented above, namely the regular 120 km mesh and the variable 60–12 km mesh. Both models are initialised in September 1981 using CFSR data (NCEP Climate Forecast System Reanalysis, Saha et al., 2010) at $0.5^\circ \times 0.5^\circ$ resolution as initial conditions. Daily updates of the sea-surface temperature are taken from the NOAA Optimum Interpolation Sea Surface Temperature Analysis (NOAA OI SST, Reynolds et al., 2002) at $0.25^\circ \times 0.25^\circ$ resolution. The period from September 1981 to beginning of 1982 is considered as spin up time for the model, in particular for the soil conditions. The model output is compared to different sets of observational data to account for the large uncertainty in the gridded observational products in the data-sparse region of West Africa (see, for example, Lorenz and Kunstmann, 2012; Sylla et al., 2013).

For near-surface air temperature and precipitation, we refer to (1) the Climate Research Unit (CRU) high-resolution gridded time-series dataset v. 3.22 (Harris et al., 2014), and (2) the University of Delaware (UDEL) Air Temperature & Precipitation long term monthly means V3.01 (Willmott and Matsuura, 2014) at $0.5^\circ \times 0.5^\circ$. Additional observational data for near-surface air temperature is obtained from the Global Historical Climate Network (GHCN) gridded 2 m temperature dataset V2 (Fan and van den Dool, 2008) at $0.5^\circ \times 0.5^\circ$. For precipitation, we also use the Global Precipitation Climatology Centre (GPCC) Full Data Reanalysis Version 6 Monthly Means (Schneider et al., 2011), also at $0.5^\circ \times 0.5^\circ$.

We also compare the MPAS-A model output to reference data obtained from a set of novel regional climate simulations over West Africa within the WASCAL program[14]. This data is produced using the regional climate model WRF at 12 km resolution with initial and lateral boundary conditions provided by the ERA-Interim re-analysis (Dee et al., 2011, 80 km resolution). The WRF model uses a setup that is optimised for the region of West Africa, following a detailed analysis of the monsoon dynamics for different WRF model configurations by Klein et al. (2015). An extensive documentation and analysis of this reference data set will be given in a forthcoming paper. The WRF model run covers a region from 25° W to 25° E and 5° S to 25° N and is initialised in January 1979. Spectral nudging is applied to the WRF limited area model to keep it on track with the large-scale features of the driving ERA-Interim re-analysis. The sea-surface temperature is updated every 6 h from the ERA-Interim SST data.

The WRF model domain lies entirely within the refinement zone of the variable 60–12 km mesh. Hence, the resolution of the MPAS-A runs is 120 km for the regular mesh (MPAS-120r hereafter) and 12 km for the variable mesh (MPAS-12v hereafter). Figure 15 shows the model topography of the WRF reference model at 12 km resolution (WRF-12r hereafter) and the MPAS-A models. Also indicated is a classification of the land area into five agro-climatical zones, which will be used in the further analysis. Naturally, the topography is nearly identical for WRF-12r and MPAS-12v. Minor differences

[14]http://www.wascal.org

GMDD
8, 6987–7061, 2015

can be seen along the coast lines and inland water bodies, which are caused by the different grids and by the need to re-grid the MPAS model output onto a regular lat-lon grid. This re-gridding is performed with an NCL[15] script `mpas_to_latlon.py` (L. Fowler, personal communication, 2014), which adds another step to the post-processing tasks and is computationally quite demanding. For example, a minimum of 1.5 GB of memory and 10 s runtime is required to re-grid one 3-D variable of MPAS-12v for one time step. For MPAS-120v, the terrain is smoothed out and the coast line (often referred to as landmask in the models) is ill-represented. This has negative effects when verifying the model output over regions such as Guinea, as we will see below.

In Fig. 16, we analyse the spatial distribution of the near-surface temperature for July 1982 (top panel) and its annual cycle between September 1981 and July 1982 (bottom panel). The observations provide data over land only and show noticeable spatial differences in the position and intensity of the Saharan Heat Low (SHL), in particular between CRU/UDEL and GHCN, and minor differences over Ghana and along the coastline. Regarding the model runs, WRF-12r matches the position and temperature of the SHL best and reproduces the observed temperatures. Both MPAS models show a slightly colder surface temperature distribution for July 1982. The cold bias in MPAS-120r is larger on average. The sea-surface temperature distribution is similar for the two MPAS runs, since they are using the same SST data for their daily updates. However, MPAS-120r shows strong artefacts along the coastline of the Golf of Guinea, which is due to its inaccurate landmask. The WRF-12r SST, which is updated every 6 h from ERA-Interim data, is colder over the Golf of Guinea, but otherwise shows the same patterns. With respect to the temporal evolution, the annual cycle is reproduced well for both MPAS models, however a significant cold bias is detected over most of the land area from the time of model initialisation in September 1981 up to May 1982. From June to July 1982, this bias seems to nearly vanish with the exception of the coarser MPAS-120v over Guinea due to the limited resolution of the coast line. The

[15]http://http://www.ncl.ucar.edu

GMDD
8, 6987–7061, 2015

MPAS: an extreme scaling experiment

D. Heinzeller et al.

observational data sets displayed in the lower panel agree in general, but show small differences for the Saharan region (only CRU and GHCN are displayed for clarity; UDEL is very close to CRU).

Figure 17 likewise displays the spatial distribution of the monthly precipitation for July 1982 (top panel) and its annual cycle (bottom panel) for the three observational data sets and the three models. At the onset of the monsoon season, the rain band is centred over 10° N for all three observational data sets. Areas of high precipitation are found over Guinea, Sierra Leone and the Senegal in the West, and over Nigeria, Cameroon and the Central African Republic in the East. While the spatial distribution hardly shows any difference between the observational data sets, the temporal evolution deviates for the Saharan and Guinea regions. For the Saharan region, small absolute values and a very small number of actual observations lead to large relative uncertainties. For Guinea, the spatial interpolation along the coast line leads to differences in the timing of the maximum precipitation (April 1982 for CRU, May 1982 for GPCC; as for temperature, UDEL follows CRU closely).

The three models successfully reproduce the location of the rain band, a fact that should not be taken for granted. In the case of WRF, Klein et al. (2015) demonstrate that the representation of the monsoon dynamics is largely determined by the microphysics and the planetary boundary layer schemes, while the cumulus scheme seems to play more of a role on daily time scales and for the actual amount of precipitation triggered by mesoscale convection. The WRF model configuration chosen here uses the WSM5 microphysics scheme, the ACM2 planetary boundary layer parameterisation and the Grell–Freitas cumulus scheme (see Wang et al., 2014, for a summary of the WRF physics options and further references). It is highly optimised for the region and thus not only matches the location of the rain band, but also reproduces the observed precipitation patterns over the Soudano, the Sahel and the Sahelo regions. The two MPAS model runs, on the other hand, use an "out-of-the-box" setup, which consists of the WSM6 microphysics scheme (similar to WSM5 with graupel as additional hydrometeor), the YSU planetary boundary layer parameterisation and the Kain–Fritsch

GMDD
8, 6987–7061, 2015

cumulus scheme. This particular combination produces excessive precipitation during the peak of the monsoon in WRF due to a non-linear response of convective precipitation events to the dynamics, and it seems to exhibit the same behaviour in the two MPAS models.

With respect to the annual cycle of precipitation, the WRF model shows excessive precipitation for all months and an early onset of the monsoon season for the Soudano, Sahel and Sahelo regions. The excess in rainfall over all land area is mainly caused by an overestimation over Guinea, which receives most rainfall over the year (more than 3000 mm day^{-1}, compared to less than 500 mm day^{-1} in the Sahelo region). The "out-of-the-box" MPAS models match the observations better, in particular the timing of the onset of the rainy season and the precipitation over Guinea. The coarser MPAS-120r is closer to the observed precipitation over the inland areas than the higher-resolution MPAS-12v during the onset of the monsoon in June/July 1982. This, however, is not a signal of a higher accuracy of the coarser model: at 120 km resolution, the Kain–Fritsch cumulus scheme is less active than at 12 km resolution, and consequently its wet bias is reduced.

To support this further, Fig. 18a displays the mean sea level pressure map for July 1982. WRF-12r and MPAS-12r both show a distinct area of low pressure, the Saharan Heat Low (SHL), alongside with the South–North pressure gradient that is causing the movement of the ITCZ and the associated monsoon rain band. This SHL is much less pronounced in MPAS-120r. In both MPAS models, the region of low pressure is displaced by about 10° to the East compared to WRF. Lavaysse et al. (2009) derive a climatological mean position of 3° W, 23° N from re-analysis data between 1979 to 2001, which coincides well with WRF.

However, the Saharan Heat Low is not only a region of low surface pressure but also of high surface temperatures. For further comparison, Fig. 20 displays the mean near-surface temperature and the mean sea level pressure for July 1982 for three selected re-analyses: CFSR (used as initial conditions for MPAS on 1 January 1981), ERA-Interim (used as lateral boundary conditions for WRF-12r with 6 hourly updates), and

NASA's Modern-Era Retrospective Analysis for Research and Applications (MERRA, Rienecker et al., 2011). All three data sets show a bimodal distribution of areas of low pressure below 1008 hPa (CFSR) or 1007 hPA (others), where the western system corresponds to the SHL and is close to the climatological mean. Large differences are visible in the corresponding near-surface temperature, with CFSR being the coldest, MERRA the warmest and ERA-Interim in-between and closest to the observations.

Comparing Fig. 16 and Fig. 18a, it is apparent that the areas of low pressure and high temperature are co-located for WRF-12r and that the model is close to reproducing the bimodal distribution of the re-analyses. The high-temperature regions of MPAS-120r and MPAS-12v match the WRF SHL position albeit a cold bias of about 2 °C, while the low-pressure region is shifted to the East and does not match the bimodal distribution. This is caused by the cold bias in the two MPAS models: the SHL, like any other non-frontal thermal low, is formed by rapid solar heating of the land surface and the near-surface layers, which leads to a rising of hot and dense air and to the formation of a stationary low pressure area. Thus, the cold bias in the MPAS models implies a less intense deepening of the pressure system at the expected location of the SHL. As discussed above, the general cold bias over all land areas persists from the onset of the MPAS model runs in September 1981 and only starts to vanish from June to July 1982 on. This is reflected in the temporal evolution of the mean sea level pressure (Fig. 19, left panel), integrated over all land areas, which is highest for MPAS-120r, lowest for WRF-12r, in-between for MPAS-12v, and merging towards each other from June 1982 on.

A final investigation of the soil properties in Figs. 18b and c and 19 (middle and right panel) reveal the root cause of the cold temperature bias and the associated displacement of the low pressure system. Starting from the MPAS model initialisation in September 1981, the soil temperature is about 2 °C lower then for the WRF model run, which is initialised in January 1979 and thus has more than 2 years to spin up the land surface model (NOAH LSM for both WRF and MPAS). Over the course of the simulated 11 months, the MPAS soil temperatures start to converge towards the

GMDD
8, 6987–7061, 2015

WRF soil temperature: in July 1982, the soil temperatures distributions in Fig. 18b are already quite similar. However, the relative soil moisture maintains a constant bias for most of the time and still shows spatial differences in July 1982. This is due to the fact that between the MPAS model initialisation in September 1981 and the onset of the monsoon season in 1982, virtually no precipitation occurs over large fractions of the land area and that the inherently low soil moisture simply has not possibility to adapt.

We therefore conclude from this section that MPAS-A is capable of reproducing the dynamics of the West African Monsoon and of the associated precipitation. The "out-of-the-box" setup of MPAS even beats the optimised WRF setup with respect to the timing of the onset of the rainy season, and the high-resolution MPAS-12v model shows better performance than the coarse-resolution MPAS-120r model in general, but in particular for the coastal regions. However, deficiencies in the placement of the Saharan Heat Low and a cold bias in the surface temperature are apparent in both MPAS model runs, which are caused to a large extend by an insufficient spin up time of the models. The MPAS runs also tend to over-estimate the monsoon precipitation, which we attribute to the combination of physical parameterisations of the "out-of-the-box" setup.

4 Extreme scaling experiment at very high resolution

In this section, we evaluate the scalability and limitations of the MPAS-A model for a very large mesh on a massively parallel system. This experiment is motivated by the following two aspects:

1. Future HPC environments will most likely be massively parallel systems, with the number of cores per node and the number of nodes increasing much faster than the speed of the individual cores. Models such as MPAS-A have to be able to scale on these systems in order to be used successfully in the future.

2. The typical model resolution of global and regional NWP and climate models has increased continuously over the past few decades. Currently, the European Cen-

tre for Medium-Range Weather Forecasts (ECMWF) is leading the field with an operational global NWP model at 14 km resolution[16], and limited area models have been taken down to sub-km resolution. With this experiment, we want to demonstrate that convection-resolving (below about 4 km grid size, see Weisman et al., 1997; Prein et al., 2013, for example), global atmospheric simulations are possible on current HPC environments.

To create a large-enough problem for these tests at a convection-resolving resolution, we use a regular, global 3 km mesh with more than 65 million horizontal grid cells and 41 vertical levels. Up to now, only a few real-data simulations on this mesh have been conducted on NCAR's Yellowstone supercomputer using a maximum of 16 384 MPI tasks (approx. 4000 owned cells per task); a set of scaling benchmarks based on an idealised case have also been run on up to 131 072 MPI tasks on Edison, a Cray XC30 at the National Energy Research Scientific Computing Center[17]. Based on our experience with the moderate scaling tests in Sect. 2, a breakdown of the parallel performance is expected between 150 owned cells per task (corresponding to 436 906 tasks) and 600 owned cells per task (109 226 tasks).

Among the four HPC sites presented earlier, only the FZJ Juqueen offers a large enough number of cores to conduct this extreme scaling experiment. With a maximum of 458 752 cores, these tests require scaling out to the full system, which is not possible during normal operations. However, following the 3rd Juqueen Tuning and Porting Workshop in February 2015, a few selected applications were invited to conduct extreme scaling tests on the full machine during a period of 24 h. The results presented in the following were obtained during this event, which is summarised in a technical report by Brömmel et al. (2015).

[16]http://www.ecmwf.int/en/forecasts/datasets/dataset-i-i-atmospheric-fields-high-resolution-forecast

[17]https://www.nersc.gov/users/computational-systems/edison

4.1 Model configuration and experiment preparation

Several modifications of the MPAS-A code are required to conduct this experiment. Firstly, it is no longer possible to use the standard NetCDF large-file format (CDF-2), since the maximum number of elements for some of the 4-D variables exceeds the internal limit of 2 billion values for any particular record. One possible solution is to use the CDF-5 extension of CDF-2, which is supported by the Parallel-NetCDF library. However, only very few applications understand this format, and initial testing on Juqueen revealed problems with reading correct data in massively parallel read operations. Another solution, which is adopted here, is to use the newer NetCDF-4 format, which supports parallel I/O through PHDF5. This requires upgrading the parallel I/O library PIO from v1.7.1 to 1.9.15, and modifying the I/O framework of the MPAS-A model code. Motivated by this study, MPAS-A v4.0, released at the time of writing, supports NetCDF-4 I/O without any need to modify the software framework.

Further, the generation of the model input data becomes a large computational problem which cannot be fit on a single machine due to time constraints and memory limitations. In MPAS release v3.1, the pre-processing of the data is partly a serial process running on one CPU core only. Hence, a parallelisation of the pre-processing is required in addition to the above changes to the I/O routines. These changes are applied to the basic MPAS-A v3.1 code, and this modified version is used in the following scaling experiments.

Another difference from the default model configuration presented in Sect. 2.2 is that each test is run for 1 h model time only. This implies that the update of the surface data (sea-surface temperature, sea-ice fraction), which occurs every 24 h in the above moderate scaling tests, is dropped. Also, with a global resolution of 3 km, it is generally agreed that no convection scheme is required, since the microphysics scheme is able to generate the convective precipitation systems on the grid scale. These modifications are reflected in the model namelist in Appendix C.

GMDD
8, 6987–7061, 2015

The pre-processing consists of two steps. First, a static data set is produced (`static.nc`), which maps invariants such as terrain height, landmask and land use classification onto the 3 km mesh. These invariant fields are required as input for the subsequent generation of the initial conditions (`init.nc`), in part because the terrain field is necessary for the generation of the height-based vertical grid. The parallel pre-processing steps require special mesh partitions, different from the partitions generated by METIS and used for the model runs. Here, both steps are conducted with 576 cores, spread across 80 nodes on the ForHLR1 to provide sufficient memory for each task. Each step takes about 1 h 15 m realtime and requires around 4.6 TB of the available 5.1 TB of memory. The resulting initial conditions file has a size of 1.2 TB and is transferred to Juqueen over the 10 Gb internet connection between the two HPC sites. Since both pre-processing steps are only required once, no further investigation or optimisation of the runtimes is attempted.

4.2 First attempts and optimisations

Initial test runs at 3 km resolution revealed previously unknown problems on the system. As described in Sect. 2.2, a bootstrapping step is required during the model initialisation to set up the grid and instruct individual tasks with whom to share information about neighbouring grid cells. In the MPAS code, this is implemented using hash tables. In order to complete the bootstrapping in a reasonable time, the hash table size (parameter `TABLESIZE`) is increased from the default value 27 183 to 6 000 000. After this adjustment, the bootstrapping step takes between 18 and 29 min on Juqueen, depending on the number of MPI tasks (see Table 1). A second bottleneck is the reading of the initial conditions file. Performance improvements for this step are achieved by setting two runtime environment variables that were presented during the tuning and porting workshop (`BGLOCKLESSMPIO_F_TYPE`, `ROMIO_HINTS`), and by optimising the number of I/O tasks. While in the previous scaling tests all tasks participate in the I/O, we find improvements when using only 128 I/O tasks per rack, with an average read performance of $1.2\,\mathrm{GB\,s^{-1}}$ on 4–28 racks and an average write performance of

0.6 GB s^{-1}, respectively. One rack contains 16 384 nodes and is often used as convenient unit instead of the large number of nodes on Juqueen.

With these optimisations, the parallel reading of the initial conditions file improves slightly with the number of tasks, since they are located in different racks. Conversely, the bootstrapping step takes longer for larger numbers of tasks. Hence, the overall model initialisation is to some degree independent of the number of tasks and takes approximately 45 min for the 3 km mesh. One notable exception here is the run on 8 racks, for which the initial I/O is only 50 % of that of the other runs. The exact reasons for this behaviour needs to be investigated, but we think that this combination of file size and I/O tasks is a sweet spot on Juqueen.

4.3 Execution of extreme scaling tests

The substantial memory requirements for the 3 km mesh do not allow to run the model on 1 or 2 racks only. The baseline for our scaling experiment is therefore the run on 4 racks (65 536 MPI tasks, 512 I/O tasks, 65 TB memory). Contrary to the model initialisation, the time integration step scales very well up to the entire machine, with a parallel efficiency of 87 % for 24 racks (393 216 tasks) compared to the baseline (see Table 1). The test run on the full system (28 racks, 458 752 tasks) shows a lower performance than the run on 24 racks and a parallel efficiency of nearly 70 %, since the MPI overhead becomes significant for only 142 owned cells per task. All scaling tests are conducted with an 18 s model integration time step for a 1 h model time. However, we find that in order to keep the model stable when starting off the 3 km mesh from initial conditions derived from a 48 km re-analysis dataset (CFSR), a more conservative time step is required. MPAS currently lacks a dynamical initialisation system (e.g., digital filters, adaptive time-stepping), which could avoid this issue. Model instabilities leading to NaNs can affect the performance in different ways: (1) the performance might increase in case if-NaN-tests may cause the code to return early from computationally intensive physics routines, or (2) the performance might decrease due to the continuous generation of floating-point exceptions. We therefore repeat the runs for 4, 8, and 16 racks with a 12 s time step to obtain a stable model run. The measured realtimes for the three 12 s runs are very close to 1.5 times the realtimes for the corresponding 18 s runs, which gives us confidence that we can scale the results for 24 and 28 racks with an 18 s time step to a 12 s time step, despite the fact that the runs with an 18 s timestep produced NaNs.

Table 1 and Fig. 21 summarise the required times of the individual steps of the 3 km runs with an 18 s integration time step. Due to walltime constraints, we only conduct runs without writing output to disk. The last column in Table 1 estimates how many hours the 3 km model can be advanced within 24 h walltime, and is calculated as follows: a 12 s model integration time step is assumed, and the realtime required is scaled from the 18 s runs by a factor of 1.5 for 24 and 28 racks, for which no 12 s runs are conducted. For a typical production run, diagnostic output files of 13 GB size are written every 3 h model time, while comprehensive output files of approximately 250 GB size are written every 24 h model time. A restart file of 2.1 TB size is written at the end of the model run. Based on a parallel write performance of 0.6 GB s^{-1}, we make a conservative estimate that roughly two hours of the 24 h walltime will be used up by writing these files to disk. Tables G1 and G2 list the file sizes and the cheapest and fastest model runs for the 3 km mesh on Juqueen.

We conclude from this extreme scaling test that the dynamical solver of MPAS scales on massively parallel systems out to hundreds of thousands of cores. Our results confirm that the model behaves similar for the 3 km mesh than for the significantly smaller problem sizes and that the parallel efficiency is limited by the same factors, namely the increasing number of halo cells and amount of communication for large number of tasks. For all tests on Juqueen, this occurs around 150 owned cells per task, which corresponds to roughly 437 000 tasks for the 3 km mesh. However, we find that the model initialisation and the disk I/O become increasingly important and at the same time difficult to improve for extremely large test cases. Compared to the model integration, the time required for the model initialisation and for reading and writing data is largely independent of the number of tasks. For a maximum walltime of 24 h on Juqueen, these steps consume up to 3 h or 10–15 % of the total job time – in other words, hundreds of thousands of CPUh. The cheapest run on Juqueen utilises 4 racks (65 536 tasks), consumes 1.3 Mio CPUh for a 24 h model integration and gives a speedup of 1.2 × realtime. For 24 racks (393 216 tasks), a speedup of 6.3 × realtime is achieved at the slightly higher expense of 1.5 Mio CPUh.

5 Conclusions

In this study, we analyse the atmospheric model MPAS-A in detail for its numerical performance and for its physical accuracy. We conduct scaling tests for three medium-size problems using regular and variable meshes of different complexity on four different HPC facilities. We confirm an overall good scaling ($\gtrsim$ 70 % parallel efficiency) of MPAS across all systems and find that a robust limit for the breakdown of the parallel performance is given by the numbers of cells owned by each task of the parallelisation. This number ranges between 150 and 600 for a parallel efficiency of 70 % when setup and I/O costs are included in the scaling, and depends on the interconnect of the system, with faster interconnects corresponding to lower values, but also on the I/O performance and the graph partitioning. Taking into account that the setup costs are amortised over longer runs, MPAS-A maintains a parallel efficiency of 80 % or better for more than 150 owned cells per task. Based on these findings, we provide numbers on the typical file sizes and optimal model configurations for conducting research and operational runs on the different HPC systems.

An in-depth analysis of the properties of different graph partitions for one of the meshes shows that the impact of non-contiguous graph partitions in form of changes in the number of halo cells is negligible for any reasonable number of tasks for a given problem size. We further employ the parallel profiling tools Scalasca and Score-P to identify the bottlenecks in the MPAS-A code when the parallel performance breaks down. Our findings confirm that most of the time in such cases is spent waiting during the communication with neighbouring tasks, but also demonstrate the negative impact that computational imbalances can have on the model performance.

We also study the accuracy of MPAS-A for one common and challenging problem in climate research, namely the capability to reproduce the dynamics of the West African Monsoon and its associated precipitation. We conduct 11 month simulations for two meshes, a regular 120 km mesh and a variable 60–12 km mesh, and compare the model output to a number of observation data sets, selected re-analyses and a reference model run. The reference model run is chosen from a novel set of regional climate simulations over West Africa within the framework of the WASCAL programme and employs the regional climate model WRF, from which MPAS inherits several aspects of the dynamical solver and all of its physical parameterisation schemes.

We find that MPAS-A is able to model the monsoon dynamics and the northwards movement of the monsoon rain band. Despite using an "out-of-the-box" configuration of the model, both runs reproduce the timing of the onset of the monsoon season better than the optimised WRF reference run. However, we find that the precipitation in the early monsoon season is overestimated, which we attribute to the choice of physics parameterisations. The MPAS model runs also show a cold bias in the near-surface temperature and consequently fail to place the Saharan Heat Low at the correct location, which we believe stems from a too short spin up time of the model. To confirm this hypothesis, longer model runs are required that span at least one entire monsoon season in order to adjust the soil conditions.

In the last part of this study, we conduct extreme scaling tests on a global 3 km mesh with more than 65 million grid cells on up to 458 752 cores on Juqueen, the IBM Bluegene/Q at the Forschungszentrum Jülich. We describe the issues that arise when attempting such an experiment for the first time – up to now, MPAS-A has been run for real-data cases, which include a full physics suite, on a maximum number of 16 384 tasks on Yellowstone – and provide solutions that allow to conduct the scaling test in the first place and improve the model performance. We find that the model scales very well up to the entire machine with a parallel performance of nearly 70 % for 458 752

GMDD
8, 6987–7061, 2015

tasks. We confirm that the limitations and rules to estimate the scaling, derived for moderate problem sizes, are also valid for the extremely large test case. This gives confidence for planning model experiments and estimating required runtimes, storage and computational resources.

Furthermore, we identify additional aspects in the model that become increasingly relevant for larger problem sizes: the model initialisation and the disk I/O. We describe strategies to improve the performance of the model, which are partly machine-dependent. We further give estimates on required runtimes and resources for conducting scientific experiments with the 3 km mesh on Juqueen.

Our next steps will be to conduct a number of longer simulation experiments on regular and variable-resolution meshes with a moderate number of grid cells. Specifically, we plan to pursue the study on the dynamics of the West African Monsoon using a variable-resolution grid such as the 60–12 km mesh and a regular grid with a similarly fine resolution. This will allow us to compare the accuracy of the model after a full spin up of the soil conditions and to assess the impact of the variable mesh on the model results. It will also allow us to study physical processes such as the teleconnection between the oceans and the African monsoon systems, and investigate the impact of climate and land use changes in a consistent approach.

In conclusion, the MPAS-A model is a novel atmospheric model that scales well on a range of architectures for small up to extremely large numbers of tasks. Based on an unstructured Voronoi mesh, it allows to conduct global simulations with local refinement regions and smooth transition in-between them. This makes it possible to study local-scale processes in regions of interest with a full coupling to the large-scale motions and a physical consistency within the model. This is demonstrated here for the example of the West African Monsoon. This study also shows that it is possible to conduct global, convection-resolving atmospheric simulations with MPAS on current and future massively parallel systems. However, it is also evident that the application of models such as MPAS for extremely large problem sizes and numbers of tasks require substantial efforts to optimise the model to the problem *and* to the machine it is run on.

GMDD
8, 6987–7061, 2015

In order to do so, interdisciplinary approaches and more intensive training of scientist on hardware, software and programming techniques are necessary.

Appendix A: MPAS compiler flags

We use the following compiler optimisation flags for the Intel compilers icc and ifort on Curie, ForHLR1 and Juropatest:

```
CFLAGS = "-O3"
FFLAGS = "-real-size 64 -O3 -convert big_endian -FR"
```

For the IBM XL compilers mpixlc_r and mpixlf95_r on Juqueen, the following flags are used:

```
CFLAGS = "-O3 -qstrict -qarch=qp -qtune=qp"
FFLAGS = "-O3 -qstrict -qarch=qp -qtune=qp -qrealsize=8"
```

Appendix B: Configuration for moderate problem sizes

The following model configuration in terms of the usual namelist (`namelist.atmosphere`) is used for the experiments in Sect. 2.3–2.5 (regular 120 km mesh, variable 100–25 km mesh, variable 60–12 km mesh). Differences in the setup (e.g., model integration time step) are indicated in namelist-style comments. Details about the structure of the namelist file and the available options can be found in the MPAS-Atmosphere Model User's Guide (Duda et al., 2014).

```
&nhyd_model
    config_dt                = 150.0 # 120km
    config_dt                = 120.0 # 100-25km
```

```
    config_dt            =  72.0 # 60-12km
    config_start_time    = '1981-09-02_00:00:00'
    config_stop_time     = '1981-09-03_00:00:00'
    config_run_duration  = '24:00:00'
    config_len_disp      = 120000.0 # 120km
    config_len_disp      =  25000.0 # 100-25km
    config_len_disp      =  12000.0 # 60-12km
/

&damping
    config_zd = 22000.0
    config_xnutr = 0.2
/

&io
    config_pio_num_iotasks = 0
    config_pio_stride = 1
/

&decomposition
   config_block_decomp_file_prefix = 'part.'
/

&restart
    config_do_restart =.true.
/

&physics
    config_frac_seaice        =.true.
```


GMDD
8, 6987–7061, 2015

```
    config_sst_update           =.true.
    config_sstdiurn_update      =.true.
    config_deepsoiltemp_update =.true.
    config_bucket_update        = '24:00:00'
    config_bucket_rainc         = 100.0
    config_bucket_rainnc        = 100.0
    config_bucket_radt          = 1.0e9
    config_microp_scheme        = 'wsm6'
    config_convection_scheme    = 'kain_fritsch'
    config_lsm_scheme           = 'noah'
    config_pbl_scheme           = 'ysu'
    config_gwdo_scheme          = 'off'
    config_radt_cld_scheme      = 'cld_incidence'
    config_radt_lw_scheme       = 'rrtmg_lw'
    config_radt_sw_scheme       = 'rrtmg_sw'
    config_sfclayer_scheme      = 'monin_obukhov'
/
```

Appendix C: Configuration for extreme scaling tests

For the 3 km extreme scaling tests on Juqueen, the following model configuration is used. For details, the reader is referred to the MPAS-Atmosphere Model User's Guide (Duda et al., 2014).

```
&nhyd_model
    config_dt           = 12.0
    config_start_time   = '1981-09-01_00:00:00'
    config_stop_time    = '1981-09-01_01:00:00'
    config_run_duration = '01:00:00'
```


GMDD
8, 6987–7061, 2015

```
    config_len_disp     = 3000.0
/

&damping
    config_zd = 22000.0
    config_xnutr = 0.2
/

&io
    config_pio_num_iotasks = 512 # for 4 racks, 128 per rack
    config_pio_stride = 128
/

&decomposition
   config_block_decomp_file_prefix = 'part.'
/

&restart
    config_do_restart =.false.
/

&physics
    config_frac_seaice         =.false.
    config_sst_update          =.false.
    config_sstdiurn_update     =.false.
    config_deepsoiltemp_update =.false.
    config_bucket_update       = '24:00:00'
    config_bucket_rainc        = 100.0
    config_bucket_rainnc       = 100.0
```


GMDD
8, 6987–7061, 2015

MPAS: an extreme scaling experiment

D. Heinzeller et al.

```
    config_bucket_radt          = 1.0e9
    config_microp_scheme        = 'wsm6'
    config_convection_scheme    = 'off'
    config_lsm_scheme           = 'noah'
    config_pbl_scheme           = 'ysu'
    config_gwdo_scheme          = 'off'
    config_radt_cld_scheme      = 'cld_incidence'
    config_radt_lw_scheme       = 'rrtmg_lw'
    config_radt_sw_scheme       = 'rrtmg_sw'
    config_sfclayer_scheme      = 'monin_obukhov'
/
```

Author contributions. All experiments in this study were carried out by D. Heinzeller with active support of M. G. Duda. The moderately-sized scaling experiments presented in Sect. 2 were designed and analysed by D. Heinzeller, while the extreme scaling experiment was designed and realised in a collaborate effort of D. Heinzeller and M. G. Duda (Sect. 4). The analysis of the model performance with respect to the representation of the West African Summer Monsoon and its associated precipitation was conducted by D. Heinzeller and H. Kunstmann (Sect. 3).

Acknowledgements. We acknowledge that the results of this research have been achieved using the PRACE Research Infrastructure resources TGCC Curie and FZJ Juqueen based in France and Germany. Access to SCC ForHLR1 was granted through a test account, and to FZJ Juropatest through an ongoing research project on FZJ Juropa. The authors acknowledge the European Centre for Medium-Range Weather Forecasts (ECMWF) for the dissemination of ERA-Interim, the National Centers for Environment Prediction (NCEP) for the dissemination of CFSR, and the Global Modeling and Assimilation Office (GMAO) and the GES DISC for the dissemination of MERRA. Further, we acknowledge the NOAA/OAR/ESRL PSD, Boulder, Colorado, USA, for providing the UDEL air temperature and precipitation, GHCN air temperature,

GMDD
8, 6987–7061, 2015

MPAS: an extreme scaling experiment

D. Heinzeller et al.

GPCC precipitation, and NOAA OI SST sea-surface temperature data sets. We also thank PRACE for funding the 3rd Juqueen Porting and Tuning Workshop 2015 as part of the PRACE Advanced Training Centres courses. The authors are particularly grateful for the extensive and valuable support of the Jülich Supercomputing Centre (JSC) support team during the extreme scaling experiment: Dirk Brömmel, Wolfgang Frings, Markus Geimer, Klaus Görgen, Sabine Grießbach, Lars Hoffmann, Catrin Meyer, Michael Rambadt, Michael Stephan, and Brian Wylie.

The article processing charges for this open-access publication were covered by a Research Centre of the Helmholtz Association.

References

Borkar, S. and Chien, A. A.: The future of microprocessors, Commun. ACM, 54, 67–77, 2011. 6992

Brömmel, D., Frings, W., and Wylie, B.: Technical Report Juqueen Extreme Scaling Workshop 2015, Tech. rep., Jülich, Germany, available at: http://hdl.handle.net/2128/8435 (last access: 25 August 2015), 2015. 7016

Caron, J.-F.: Mismatching perturbations at the lateral boundaries in limited-area ensemble forecasting: a case study, Mon. Weather Rev., 141, 356–374, doi:10.1175/MWR-D-12-00051.1, 2013. 6990

Caya, D. and Biner, S.: Internal variability of RCM simulations over an annual cycle, Clim. Dynam., 22, 33–46, doi:10.1007/s00382-003-0360-2, 2004. 6990

Davies, H. C.: Limitations of some common lateral boundary schemes used in regional NWP models, Mon. Weather Rev., 111, 1002–1012, doi:10.1175/1520-0493(1983)111<1002:LOSCLB>2.0.CO;2, 1983. 6989

Dee, D. P., Uppala, S. M., Simmons, A. J., Berrisford, P., Poli, P., Kobayashi, S., Andrae, U., Balmaseda, M. A., Balsamo, G., Bauer, P., Bechtold, P., Beljaars, A. C. M., van de Berg, L., Bidlot, J., Bormann, N., Delsol, C., Dragani, R., Fuentes, M., Geer, A. J., Haimberger, L., Healy, S. B., Hersbach, H., Hólm, E. V., Isaksen, L., Kållberg, P., Köhler, M., Matricardi, M., Mcnally, A. P., Monge-Sanz, B. M., Morcrette, J. J., Park, B. K., Peubey, C. de Rosnay, P., Tavolato, C., Thépaut, J. N., and Vitart, F.: The ERA-Interim reanalysis: configuration

GMDD
8, 6987–7061, 2015
MPAS: an extreme scaling experiment
D. Heinzeller et al.

and performance of the data assimilation system, Q. J. Roy. Meteor. Soc., 137, 553–597, doi:10.1002/qj.828, 2011. 7010

Dennis, J. M., Edwards, J., Jacob, R., Loy, R., Mirin, A., and Vertenstein, M.: Parallel I/O library (PIO), available at: http://www.cesm.ucar.edu/models/pio (last access: 25 August 2015), 2013. 6998

Du, Q., Gunzburger, M. D., and Ju, L.: Constrained centroidal voronoi tessellations for surfaces, SIAM J. Sci. Comput., 24, 1488–1506, doi:10.1137/S1064827501391576, 2003. 6991

Duda, M., Fowler, L., Skamarock, W., Roesch, C., Jacobsen, D., and Ringler, T.: MPAS-Atmosphere Model User's Guide Version 3.0, available at: http://www2.mmm.ucar.edu/projects/mpas/mpas_atmosphere_users_guide_3.0.pdf (last access: 25 August 2015), 2014. 7024, 7026

Fan, Y. and van den Dool, H.: A global monthly land surface air temperature analysis for 1948–present, J. Geophys. Res.-Atmos., 113, D01103, doi:10.1029/2007JD008470, 2008. 7010

Grist, J. P. and Nicholson, S. E.: A study of the dynamic factors influencing the rainfall variability in the West African Sahel, J. Climate, 14, 1337–1359, doi:10.1175/1520-0442(2001)014<1337:ASOTDF>2.0.CO;2, 2001. 6993

Harris, I., Jones, P. D., Osborn, T. J., and Lister, D. H.: Updated high-resolution grids of monthly climatic observations – the CRU TS3.10 Dataset, Int. J. Climatol., 34, 623–642, doi:10.1002/joc.3711, 2014. 7010

Harris, L. M. and Durran, D. R.: An idealized comparison of one-way and two-way grid nesting, Mon. Weather Rev., 138, 2174–2187, doi:10.1175/2010MWR3080.1, 2010. 6989

Hourdin, F., Musat, I., Guichard, F., Ruti, P. M., Favot, F., Filiberti, M. A., Pham, M. A. I., Grandpeix, J. Y., Polcher, J. A. N., Marquet, P., Boone, A., Lafore, J. P., Redelsperger, J. L., Dell'Aquila, A., Doval, T. L., Traore, A. K., and Gallée, H.: Amma-Model intercomparison project, B. Am. Meteorol. Soc., 91, 95–104, doi:10.1175/2009BAMS2791.1, 2010. 6993

Karypis, G. and Kumar, V.: Multilevel *k* way partitioning scheme for irregular graphs, J. Parallel Distr. Com., 48, 96–129, 1998. 6997

Klein, C., Heinzeller, D., Bliefernicht, J., and Kunstmann, H.: Variability of West African monsoon patterns generated by a WRF multi-physics ensemble, Clim. Dynam., doi:10.1007/s00382-015-2505-5, online first, 2015. 6993, 7009, 7010, 7012

Klemp, J. B.: A terrain-following coordinate with smoothed coordinate surfaces, Mon. Weather Rev., 139, 2163–2169, doi:10.1175/MWR-D-10-05046.1, 2011. 6991

Laprise, R.: Resolved scales and nonlinear interactions in limited-area models, J. Atmos. Sci., 60, 768–779, doi:10.1175/1520-0469(2003)060<0768:RSANII>2.0.CO;2, 2003. 6989

Lavaysse, C., Flamant, C., Janicot, S., Parker, D. J., Lafore, J. P., Sultan, B., and Pelon, J.: Seasonal evolution of the West African heat low: a climatological perspective, Clim. Dynam., 33, 313–330, doi:10.1007/s00382-009-0553-4, 2009. 7013

Leduc, M. and Laprise, R.: Regional climate model sensitivity to domain size, Clim. Dynam., 32, 833–854, doi:10.1007/s00382-008-0400-z, 2008. 6990

Lorenz, C. and Kunstmann, H.: The hydrological cycle in three state-of-the-art reanalyses: intercomparison and performance analysis, J. Hydrometeorol., 13, 1397–1420, doi:10.1175/JHM-D-11-088.1, 2012. 7009

MacDonald, A. E., Middlecoff, J., Henderson, T., and Lee, J.-L.: A general method for modeling on irregular grids, Int. J. High Perform. C., 25, 392–403, doi:10.1177/1094342010385019, 2011. 6992

Miguez-Macho, G., Stenchikov, G. L., and Robock, A.: Spectral nudging to eliminate the effects of domain position and geometry in regional climate model simulations, J. Geophys. Res.-Atmos., 109, D13104, doi:10.1029/2003JD004495, 2004. 6990

Nicholson, S. E. and Webster, P. J.: A physical basis for the interannual variability of rainfall in the Sahel, Q. J. Roy. Meteor. Soc., 133, 2065–2084, doi:10.1002/qj.104, 2007. 6993

Nikulin, G., Jones, C., Giorgi, F., Asrar, G., Büchner, M., Cerezo-Mota, R., Christensen, O. B. s., Déqué, M., Fernandez, J., Hänsler, A., van Meijgaard, E., Samuelsson, P., Sylla, M. B., and Sushama, L.: Precipitation climatology in an ensemble of CORDEX-Africa regional climate simulations, J. Climate, 25, 6057–6078, doi:10.1175/JCLI-D-11-00375.1, 2012. 6989, 6993

Park, S.-H., Klemp, J. B., and Skamarock, W. C.: A comparison of mesh refinement in the global MPAS-A and WRF models using an idealized normal-mode baroclinic wave simulation, Mon. Weather Rev., 142, 3614–3634, 2014. 6989, 6990

Prein, A. F., Gobiet, A., Suklitsch, M., Truhetz, H., Awan, N. K., Keuler, K., and Georgievski, G.: Added value of convection permitting seasonal simulations, Clim. Dynam., 41, 2655–2677, doi:10.1007/s00382-013-1744-6, 2013. 7016

Reynolds, R. W., Rayner, N. A., Smith, T. M., Stokes, D. C., and Wang, W.: An improved in situ and satellite SST analysis for climate, J. Climate, 15, 1609–1625, doi:10.1175/1520-0442(2002)015<1609:AIISAS>2.0.CO;2, 2002. 7009

Rienecker, M. M., Suarez, M. J., Gelaro, R., Todling, R., Bacmeister, J., Liu, E., Bosilovich, M. G., Schubert, S. D., Takacs, L., Kim, G. K., Bloom, S., Chen, J., Collins, D., Conaty, A., Da Silva, A., Gu, W., Joiner, J., Koster, R. D., Lucchesi, R., Molod, A., Owens, T., Pawson, S., Pegion, P., Redder, C. R., Reichle, R., Robertson, F. R., Ruddick, A. G., Sienkiewicz, M., and Woollen, J.: MERRA: NASA's modern-era retrospective analysis for research and applications, J. Climate, 24, 3624–3648, doi:10.1175/JCLI-D-11-00015.1, 2011. 7014

Ringler, T. D., Thuburn, J., and Klemp, J.: A unified approach to energy conservation and potential vorticity dynamics for arbitrarily-structured C-grids, J. Comput. Phys., 229, 3065–3090, 2010. 6991

Ringler, T. D., Jacobsen, D., Gunzburger, M., Ju, L., Duda, M., and Skamarock, W.: Exploring a multiresolution modeling approach within the shallow-water equations, Mon. Weather Rev., 139, 3348–3368, doi:10.1175/MWR-D-10-05049.1, 2011. 6990

Ringler, T. D., Petersen, M., Higdon, R. L., Jacobsen, D., Jones, P. W., and Maltrud, M.: A multi-resolution approach to global ocean modeling, Ocean Model., 69, 211–232, doi:10.1016/j.ocemod.2013.04.010, 2013. 6991

Rodwell, M. J. and Hoskins, B. J.: Monsoons and the dynamics of deserts, Q. J. Roy. Meteor. Soc., 122, 1385–1404, doi:10.1002/qj.49712253408, 1996. 6993

Saha, S., Moorthi, S., Pan, H. L., Wu, X., Wang, J., Nadiga, S., Tripp, P., Kistler, R., Woollen, J., Behringer, D., Liu, H., Stokes, D., Grumbine, R., Gayno, G., Wang, J., Hou, Y. T., Chuang, H. Y., Juang, H. M. H., Sela, J., Iredell, M., Treadon, R., Kleist, D., Van Delst, P., Keyser, D., Derber, J., Ek, M., Meng, J., Wei, H., Yang, R., Lord, St., Van Den Dool, H., Kumar, A., Wang, W., Long, C., Chelliah, M., Xue, Y., Huang, B., Schemm, J. K., Ebisuzaki, W., Lin, R., Xie, P., Chen, M., Zhou, S., Higgins, W., Zou, C. Z., Liu, Q., Chen, Y., Han, Y., Cucurull, L., Reynolds, R. W., Rutledge, G., Goldberg, M.: The NCEP climate forecast system reanalysis, B. Am. Meteorol. Soc., 91, 1015–1057, doi:10.1175/2010BAMS3001.1, 2010. 7009

Schneider, U., Becker, A., Finger, P., Meyer-Christoffer, A., Rudolf, B., and Ziese, M.: GPCC full data reanalysis version 6.0 at 0.5°: monthly land-surface precipitation from rain-gauges built on GTS-based and historic data, MIMEO, doi:10.5676/DWD_GPCC/FD_M_V6_050, 2011. 7010

Skamarock, W., Klemp, J., Dudhi, J., Gill, D., Barker, D., Duda, M., Huang, X.-Y., Wang, W., and Powers, J.: A Description of the Advanced Research WRF Version 3, NCAR Technical Note NCAR/TN-468+STR, doi:10.5065/D6DZ069T, 2008. 6991

Skamarock, W. C., Klemp, J. B., Duda, M. G., Fowler, L. D., Park, S.-H., and Ringler, T. D.: A multiscale nonhydrostatic atmospheric model using centroidal voronoi tesselations and

C-grid staggering, Mon. Weather Rev., 140, 3090–3105, doi:10.1175/MWR-D-11-00215.1, 2012. 6991, 6992, 7041

Smiatek, G., Kunstmann, H., Knoche, R., and Marx, A.: Precipitation and temperature statistics in high-resolution regional climate models: evaluation for the European Alps, J. Geophys. Res., 114, D19107, doi:10.1029/2008JD011353, 2009. 6989

Staniforth, A.: Regional modeling: a theoretical discussion, Meteorol. Atmos. Phys., 63, 15–29, doi:10.1007/BF01025361, 1997. 6989

Sultan, B., Janicot, S., and Diedhiou, A.: The West African monsoon dynamics. Part I: Documentation of intraseasonal variability, J. Climate, 16, 3389–3406, doi:10.1175/1520-0442(2003)016<3389:TWAMDP>2.0.CO;2, 2003. 6993

Sylla, M. B., Gaye, A. T., Jenkins, G. S., Pal, J. S., and Giorgi, F.: Consistency of projected drought over the Sahel with changes in the monsoon circulation and extremes in a regional climate model projections, J. Geophys. Res.-Atmos., 115, D16108, doi:10.1029/2009JD012983, 2010. 6993

Sylla, M. B., Giorgi, F., Coppola, E., and Mariotti, L.: Uncertainties in daily rainfall over Africa: assessment of gridded observation products and evaluation of a regional climate model simulation, Int. J. Climatol., 33, 1805–1817, doi:10.1002/joc.3551, 2013. 7009

Thuburn, J., Ringler, T. D., Skamarock, W. C., and Klemp, J. B.: Numerical representation of geostrophic modes on arbitrarily structured C-grids, J. Comput. Phys., 228, 8321–8335, doi:10.1016/j.jcp.2009.08.006, 2009. 6991

von Storch, H., Langenberg, H., and Feser, F.: A spectral nudging technique for dynamical downscaling purposes, Mon. Weather Rev., 128, 3664–3673, doi:10.1175/1520-0493(2000)128<3664:ASNTFD>2.0.CO;2, 2000. 6990

Wang, W., Bruyère, C., Duda, M., Dudhia, J., Gill, D., Kavulich, M., Keene, K., Lin, H.-C., Michalakes, J., Rizvi, S., Zhang, X., Berner, J., Smith, K., Beezley, J. D., Coen, J. L., Mandel, J., Chuang, H.-Y., McKee, N., Slovacek, T., and Wolff, J.: WRF Users Guide, available at: http://www2.mmm.ucar.edu/wrf/users/docs/user_guide_V3/ARWUsersGuideV3.pdf (last access: 25 August 2015), 2014. 7012

Warner, T. T., Peterson, R. A., and Treadon, R. E.: A tutorial on lateral boundary conditions as a basic and potentially serious limitation to regional numerical weather prediction, B. Am. Meteorol. Soc., 78, 2599–2617, doi:10.1175/1520-0477(1997)078<2599:ATOLBC>2.0.CO;2, 1997. 6989

GMDD
8, 6987–7061, 2015

Weisman, M. L., Skamarock, W. C., and Klemp, J. B.: The resolution dependence of explicitly modeled convective systems, Mon. Weather Rev., 125, 527–548, doi:10.1175/1520-0493(1997)125<0527:TRDOEM>2.0.CO;2, 1997. 7016

Willmott, C. and Matsuura, K.: University of Delaware Air Temperature and Precipitation, Long Term Monthly Means V3.01, available at: http://www.esrl.noaa.gov/psd/data/gridded/data.UDel_AirT_Precip.html (last access: 25 August 2015), 2014. 7010

Zaengel, G., Reinert, D., Rípodas, P., and Baldauf, M.: The ICON (ICOsahedral Non-hydrostatic) modelling framework of DWD and MPI-M: description of the non-hydrostatic dynamical core, Q. J. Roy. Meteor. Soc., 141, 563–579, 2015. 6990

GMDD

8, 6987–7061, 2015

MPAS: an extreme scaling experiment

D. Heinzeller et al.

Table 1. MPAS-A 3 km global simulation experiment (strong scaling tests).

Nodes	Tasks (MPI only)	Bootstrapping [s]	Initial read [s]
4096	65 536	1260	1260
8192	131 072	1370	590
16 384	262 144	1560	1020
24 576	393 216	1680	1080
28 672	458 752	1740	1140
Nodes	**Integration time f. 1 h model time [s]**	**Parallel efficiency integration only**	**Integration in 24 h walltime***
4096	1760	100.0 %	29 h
8192	960	91.2 %	53 h
16 384	490	90.1 %	104 h
24 576	335	87.7 %	152 h
28 672	360	69.5 %	141 h

* Estimated time extrapolated from 1 h integration, including initial bootstrapping/reading, output to disk, 12 s time step

GMDD
8, 6987–7061, 2015
MPAS: an extreme scaling experiment
D. Heinzeller et al.

Table D1. Scaling tests for the 120 km regular mesh on the four HPC sites.

HPC site	Nodes	Tasks	Realtime [s] per 24 h	CPUh per 24 h	Parallel efficiency	Cells/ task
Curie	1	16	1306	5.8	100.0 %	2560
	2	32	633	5.6	103.16 %	1280
	4	64	377	6.7	86.6 %	640
	6	96	305	8.1	71.37 %	427
	8	128	269	9.6	60.69 %	320
	10	160	236	10.5	55.34 %	256
	12	192	212	11.3	51.34 %	213
	16	256	187	13.3	43.65 %	160
	24	384	182	19.4	29.9 %	107
	32	512	181	25.7	22.55 %	80
ForHLR1	1	20	863	4.8	100.0 %	2048
	2	40	486	5.4	88.79 %	1024
	3	60	317	5.3	90.75 %	683
	4	80	255	5.7	84.61 %	512
	6	120	190	6.3	75.7 %	341
	8	160	149	6.6	72.4 %	256
	10	200	135	7.5	63.93 %	205
	12	240	128	8.5	56.18 %	171
	16	320	127	11.3	42.47 %	128
	18	360	131	13.1	36.6 %	114
	20	400	130	14.4	33.19 %	102
Jtest-full	1	28	651	5.1	100.0 %	1463
	2	56	333	5.2	97.75 %	731
	4	112	177	5.5	91.95 %	366
	6	168	133	6.2	81.58 %	244
	8	224	109	6.8	74.66 %	183
	10	280	102	7.9	63.82 %	146
	12	336	92	8.6	58.97 %	122
	15	420	91	10.6	47.69 %	98
Jtest-half	1	14	1172	9.1	100.0 %	2926
	2	28	628	9.8	93.31 %	1463
	4	56	317	9.9	92.43 %	731
	6	84	220	10.3	88.79 %	488
	8	112	167	10.4	87.72 %	366
	10	140	142	11.0	82.54 %	293
	15	210	95	11.1	82.25 %	195
	20	280	87	13.5	67.36 %	146
	25	350	88	17.1	53.27 %	117
	30	420	99	23.1	39.46 %	98
Juqueen	32	512	661	94.0	100.0 %	80
	64	1024	477	135.7	69.29 %	40
	96	1536	586	250.0	37.6 %	27
	128	2048	608	345.9	27.18 %	20
	192	3072	751	640.9	14.67 %	13

GMDD
8, 6987–7061, 2015

Table E1. Scaling tests for the 100–25 km variable mesh on the four HPC sites.

HPC site	Nodes	Tasks	Realtime [s] per 24 h	CPUh per 24 h	Parallel efficiency	Cells/ task
Curie	1	16	6086	27.05	100.0 %	10 240
	4	64	1528	27.16	99.57 %	2560
	8	128	782	27.8	97.28 %	1280
	16	256	424	30.15	89.71 %	640
	24	384	314	33.49	80.76 %	427
	32	512	265	37.69	71.77 %	320
	48	768	223	47.57	56.86 %	213
	64	1024	263	74.81	36.16 %	160
	96	1536	271	115.63	23.39 %	107
	128	2048	293	166.68	16.23 %	80
	192	3072	541	461.65	5.86 %	53
ForHLR1	1	20	4413	24.52	100.0 %	8192
	4	80	1129	25.09	97.72 %	2048
	8	160	555	24.67	99.39 %	1024
	10	200	474	26.33	93.1 %	819
	15	300	346	28.83	85.03 %	546
	20	400	316	35.11	69.83 %	410
	25	500	257	35.69	68.68 %	328
	30	600	239	39.83	61.55 %	273
	40	800	253	56.22	43.61 %	205
	45	900	196	49.0	50.03 %	182
	50	1000	208	57.78	42.43 %	164
	55	1100	217	66.31	36.98 %	149
	60	1200	210	70.0	35.02 %	137
Jtest-full	1	28	3361	26.14	100.0 %	5852
	2	56	1644	25.57	102.22 %	2926
	4	112	807	25.11	104.12 %	1463
	8	224	418	26.01	100.51 %	731
	10	280	349	27.14	96.3 %	585
	15	420	260	30.33	86.18 %	390
	20	560	215	33.44	78.16 %	293
	25	700	186	36.17	72.28 %	234
	30	840	168	39.2	66.69 %	195
	40	1120	180	56.0	46.68 %	146
	50	1400	186	72.33	36.14 %	117
Jtest-half	1	14	5405	42.04	100.0 %	11 703
	2	28	2766	43.03	97.7 %	5852
	4	56	1487	46.26	90.87 %	2926
	8	112	734	45.67	92.05 %	1463
	10	140	620	48.22	87.18 %	1170
	15	210	407	47.48	88.53 %	780
	20	280	323	50.24	83.67 %	585
	30	420	233	54.37	77.32 %	390
	40	560	286	88.98	47.25 %	293
	50	700	229	89.06	47.21 %	234
	55	770	226	96.68	43.48 %	213
Juqueen	32	512	2250	320.0	100.0 %	320
	64	1024	1365	388.27	82.42 %	160
	96	1536	1323	564.48	56.69 %	107
	128	2048	1168	664.46	48.16 %	80
	160	2560	1004	713.96	44.82 %	64
	192	3072	940	802.13	39.89 %	53
	256	4096	700	796.44	40.18 %	40
	384	6144	554	945.49	33.84 %	27
	512	8192	562	1278.86	25.02 %	20
	1024	16 384	1749	7959.89	4.02 %	10

Table F1. Scaling tests for the 60–12 km variable mesh on the four HPC sites.

HPC site	Nodes	Tasks	Realtime [s] per 24 h	CPUh per 24 h	Parallel efficiency	Cells/ task
Curie	1	16	27 428	121.9	100.0 %	33 472
	4	64	7715	137.2	88.88 %	8368
	8	128	3955	140.6	86.69 %	4184
	16	256	2025	144.0	84.65 %	2092
	24	384	1349	143.9	84.72 %	1395
	48	768	777	165.8	73.54 %	697
	64	1024	690	196.3	62.11 %	523
	96	1536	567	241.9	50.39 %	349
	128	2048	484	275.3	44.27 %	262
	192	3072	505	430.9	28.29 %	174
	256	4096	628	714.5	17.06 %	131
	384	6144	604	1030.8	11.83 %	87
ForHLR1	2	40	10 967	121.9	100.0 %	13 389
	4	80	5645	125.4	97.14 %	6694
	8	160	2876	127.8	95.33 %	3347
	15	300	1584	132.0	92.31 %	1785
	20	400	1234	137.1	88.87 %	1339
	30	600	922	153.7	79.3 %	893
	40	800	720	160.0	76.16 %	669
	50	1000	704	195.6	62.31 %	536
	60	1200	649	216.3	56.33 %	446
	80	1600	635	282.2	43.18 %	335
	100	2000	543	301.7	40.39 %	268
	120	2400	459	306.0	39.82 %	223
Jtest-full	1	28	17 151	133.4	100.0 %	19 127
	2	56	8552	133.0	100.27 %	9563
	8	224	2106	131.0	101.8 %	2391
	10	280	1704	132.5	100.65 %	1913
	15	420	1113	129.9	102.73 %	1275
	20	560	862	134.1	99.48 %	956
	25	700	716	139.2	95.82 %	765
	30	840	613	143.0	93.26 %	638
	40	1120	507	157.7	84.57 %	478
	50	1400	437	169.9	78.49 %	383
	55	1540	428	183.1	72.86 %	348
Jtest-half	1	14	29 000	225.6	100.0 %	38 254
	2	28	14 487	225.4	100.09 %	19 127
	4	56	7143	222.2	101.5 %	9563
	8	112	4126	256.7	87.86 %	4782
	10	140	2833	220.3	102.36 %	3825
	15	210	2133	248.9	90.64 %	2550
	20	280	1583	246.2	91.6 %	1913
	30	420	1097	256.0	88.12 %	1275
	40	560	784	243.9	92.47 %	956
	50	700	624	242.7	92.95 %	765
	55	770	621	265.7	84.91 %	696
Juqueen	32	512	11 800	1678.2	100.0 %	1046
	64	1024	6950	1976.9	84.89 %	523
	96	1536	4490	1915.7	87.6 %	349
	128	2048	4100	2332.4	71.95 %	262
	192	3072	2991	2552.3	65.75 %	174
	256	4096	2979	3389.4	49.51 %	131
	384	6144	2514	4290.6	39.11 %	87
	512	8192	2468	5616.1	29.88 %	65
	640	10 240	4462	12 691.9	13.22 %	52
	1024	16 384	9863	44 887.6	3.74 %	33

GMDD
8, 6987–7061, 2015

Table G1. File sizes of input (I) and output (O) files for all meshes (uncompressed netCDF3/4). For a given mesh with n grid cells, an estimate of the required file sizes is calculated from the other runs.

Mesh	Cells	`init.nc` (I)	`diag.nc` (O)	`restart.nc` (O)	`output.nc` (O)
120 km	40 962	758 MB	8.7 MB	1.6 GB	153 MB
100–25 km	163 842	3.0 GB	33 MB	6.0 GB	597 GB
60–12 km	535 554	9.7 GB	107 MB	20 GB	2.0 GB
3 km	65 536 002	1.2 TB	13 GB	2.4 TB	250 GB
	n	19.7 kB × n	0.22 kB × n	38.8 kB × n	4.0 kB × n

GMDD
8, 6987–7061, 2015

Table G2. Summary of the scaling tests: cheapest and fastest model run configurations for a 24 h model integration with disk I/O enabled (rt = realtime).

HPC site	Nodes cheapest run	CPUh cheapest run	Nodes fastest run	Speedup fastest run
Regular 120 km mesh				
Curie	2	5.6	32	477 × rt
ForHLR1	1	4.8	12	675 × rt
Juqueen	32	94.0	64	181 × rt
Jtest-half	1	9.1	20	993 × rt
Jtest-full	1	5.1	15	949 × rt
Variable 100–25 km mesh				
Curie	1	27.1	48	387 × rt
ForHLR1	1	24.5	45	441 × rt
Juqueen	32	320	384	156 × rt
Jtest-half	1	42.0	50	488 × rt
Jtest-full	4	25.1	30	514 × rt
Variable 60–12 km mesh				
Curie	1	122	128	179 × rt
ForHLR1	2	122	120	188 × rt
Juqueen	32	1678	512	35 × rt
Jtest-half	3	216	55	139 × rt
Jtest-full	15	130	55	202 × rt
Regular 3 km mesh				
Juqueen	4096	1.3 Mio	24 576	6.3 × rt

GMDD
8, 6987–7061, 2015

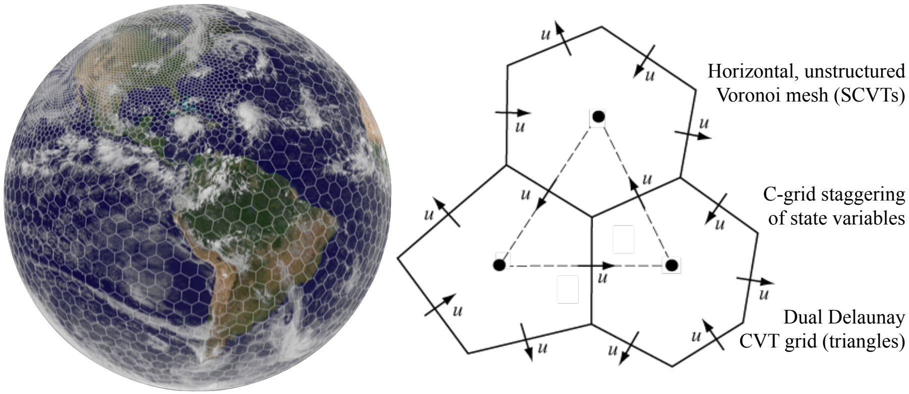

Figure 1. (left) Voronoi mesh used for the horizontal grid; (right) C-grid staggering of state variables (adapted from Skamarock et al., 2012).

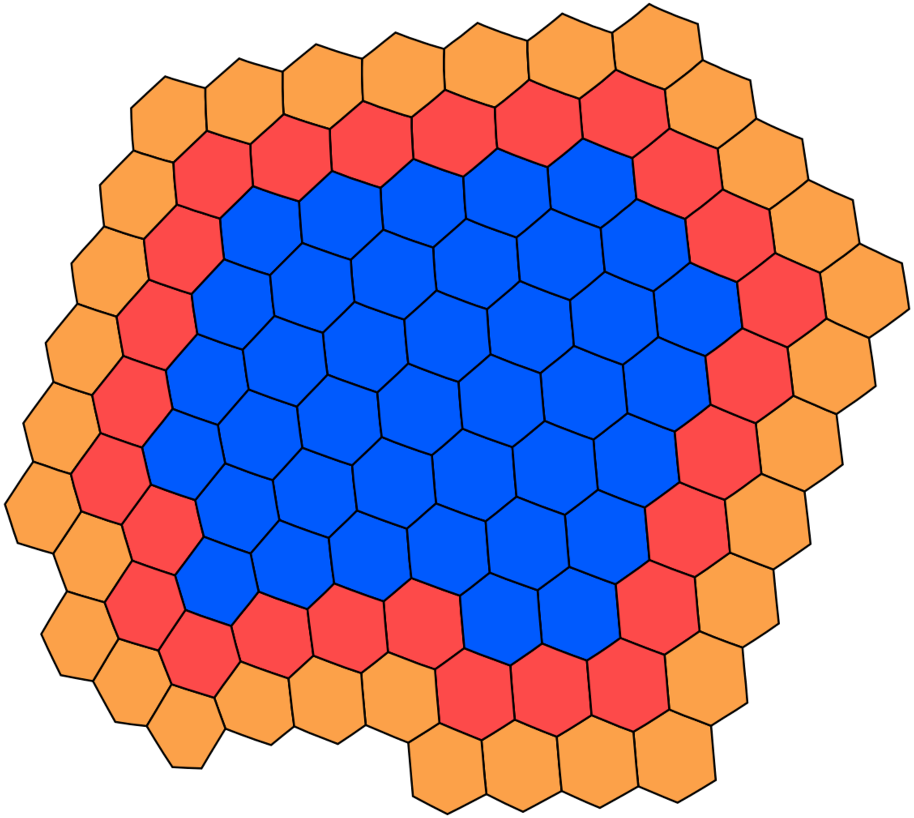

Figure 2. A block of owned cells (blue) assigned to an MPI task, along with two layers of halo cells (red, orange).

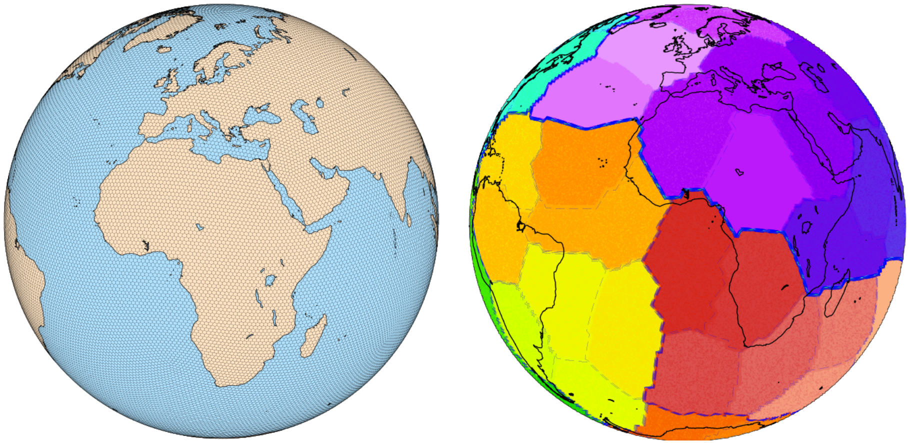

Figure 3. (left) Regular 120 km mesh with 40 962 grid cells; (right) partitioning for 64 tasks.

GMDD

8, 6987–7061, 2015

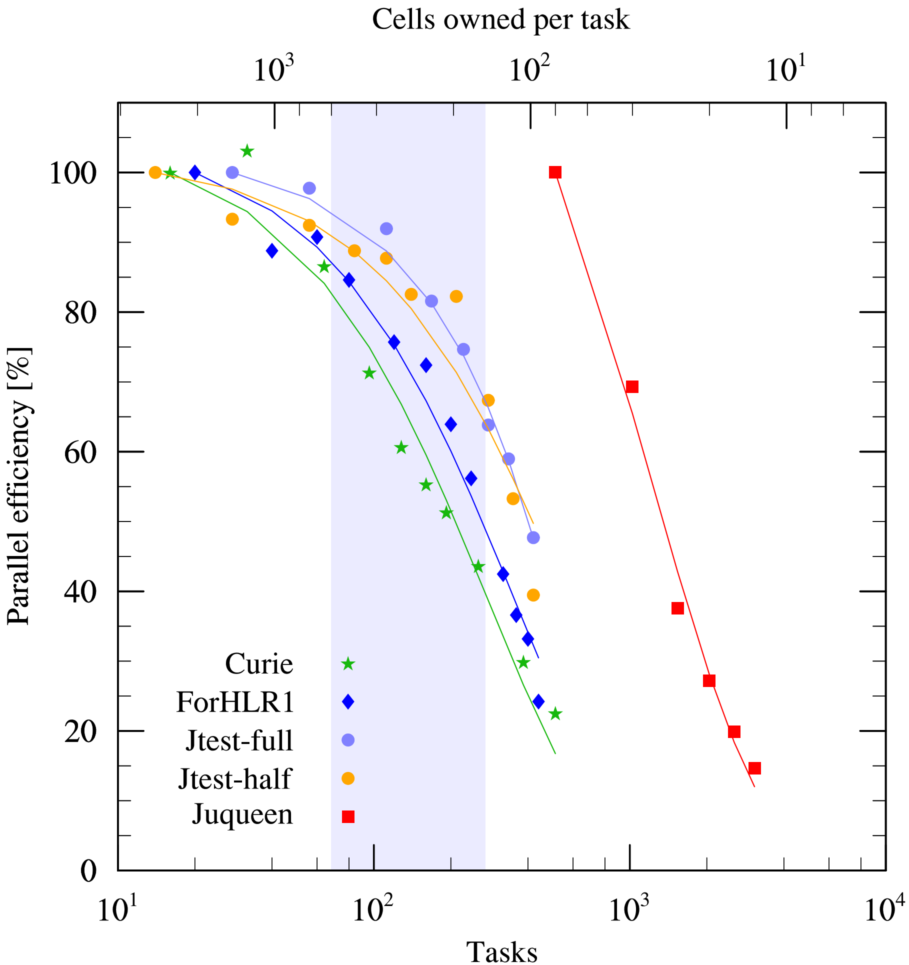

Figure 4. Scaling of the 120 km regular mesh test case.

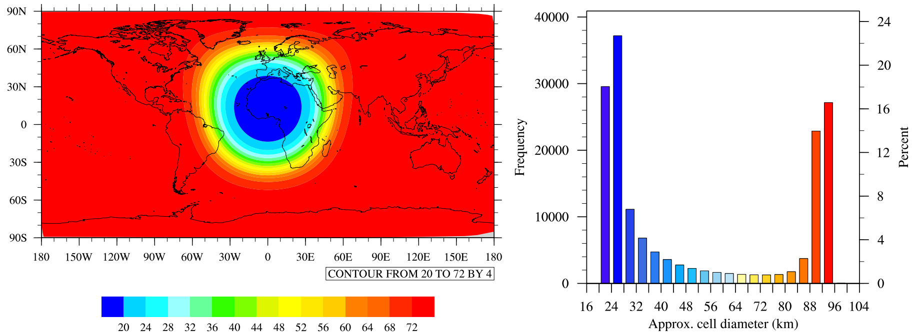

Figure 5. (left) Approximate mesh cell sizes of the variable 100–25 km mesh with 163 842 grid cells; (right) distribution of mesh cell sizes.

GMDD
8, 6987–7061, 2015

MPAS: an extreme scaling experiment

D. Heinzeller et al.

Title Page
Abstract Introduction
Conclusions References
Tables Figures
◀I ▶I
◀ ▶
Back Close
Full Screen / Esc
Printer-friendly Version
Interactive Discussion

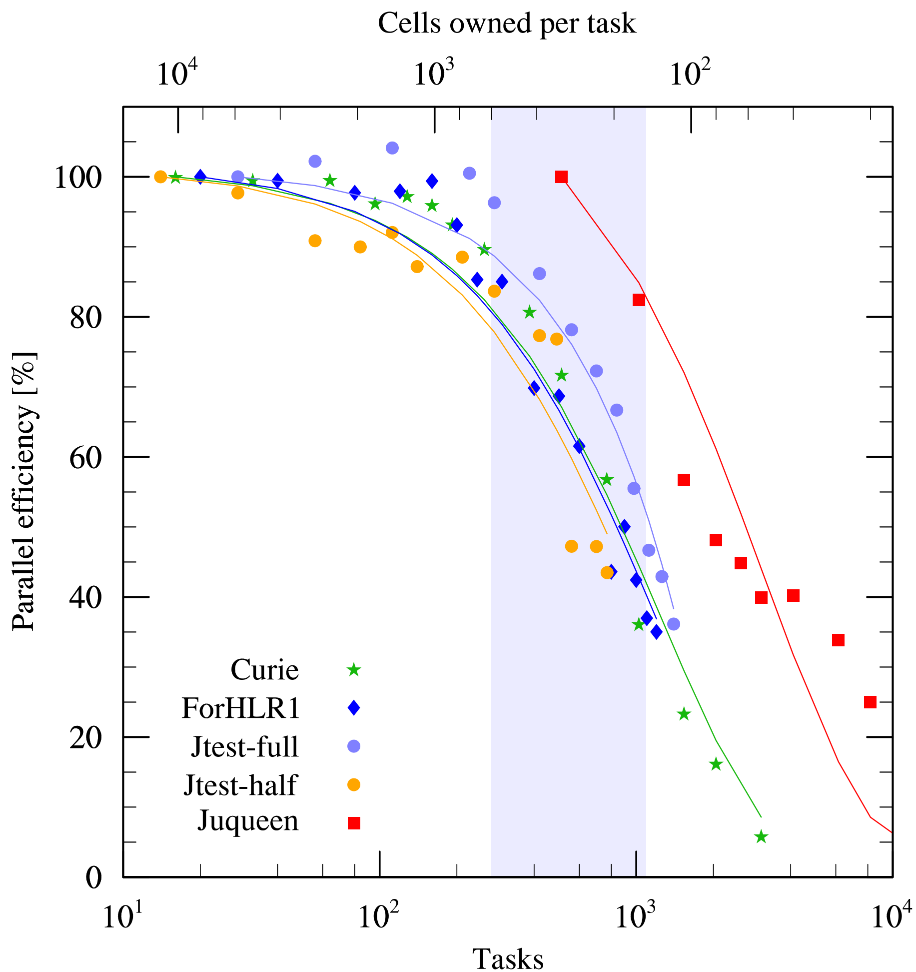

Figure 6. Scaling of the 100–25 km variable mesh test case.

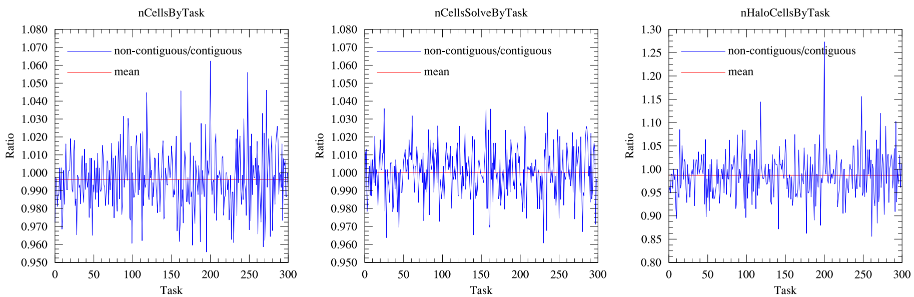

Figure 7. Ratio of (left) total number of cells, (mid) number of owned cells, and (right) number of halo cells per task between the non-contiguous and the contiguous graph partition of the variable 100–25 km mesh for 300 tasks.

GMDD
8, 6987–7061, 2015

MPAS: an extreme scaling experiment

D. Heinzeller et al.

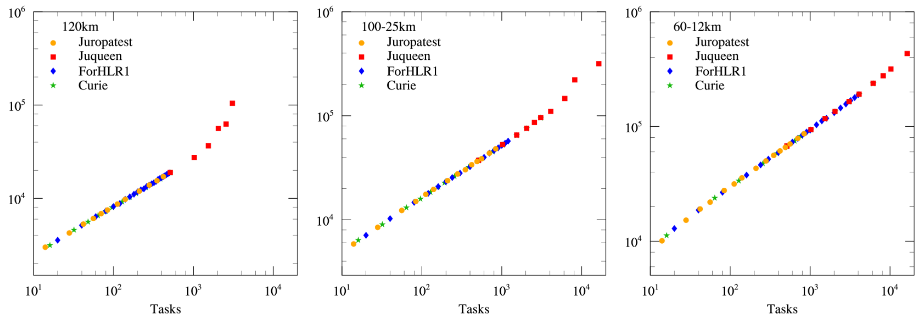

Figure 8. Communication volume as function of number of tasks for the three test cases (left: 120 km; middle: 100–25 km; right: 60–12 km). For large numbers of tasks, the relationship becomes non-linear.

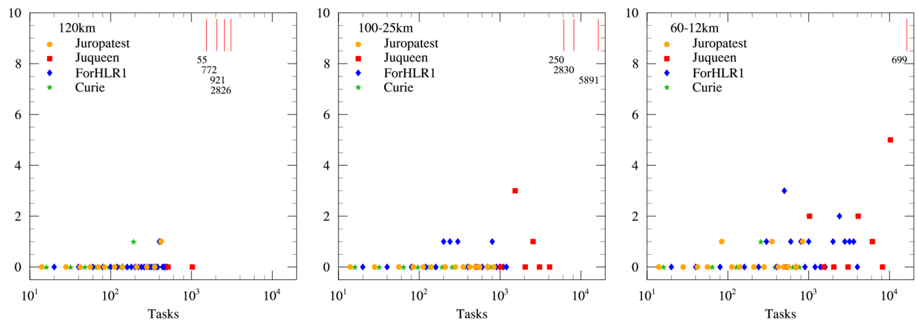

Figure 9. Number of non-contiguous partitions for the three test cases (left: 120 km; middle: 100–25 km; right: 60–12 km). For Juqueen, highly non-contiguous partitions occurring for large numbers of tasks are indicated with red lines.

GMDD
8, 6987–7061, 2015

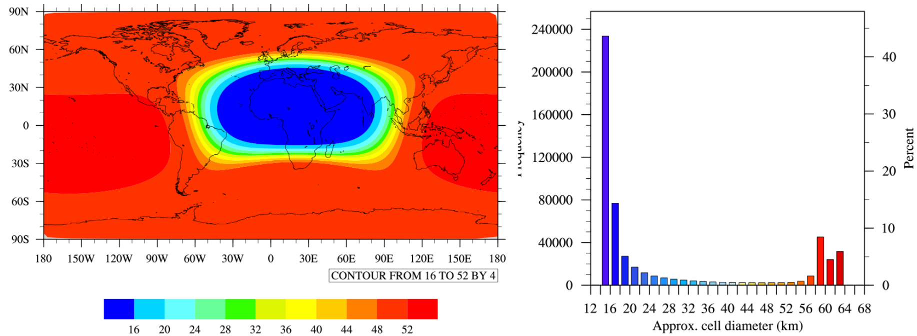

Figure 10. (left) Approximate mesh cell sizes of the variable 60–12 km mesh with 535 554 grid cells; (right) distribution of mesh cell sizes.

GMDD
8, 6987–7061, 2015

MPAS: an extreme scaling experiment

D. Heinzeller et al.

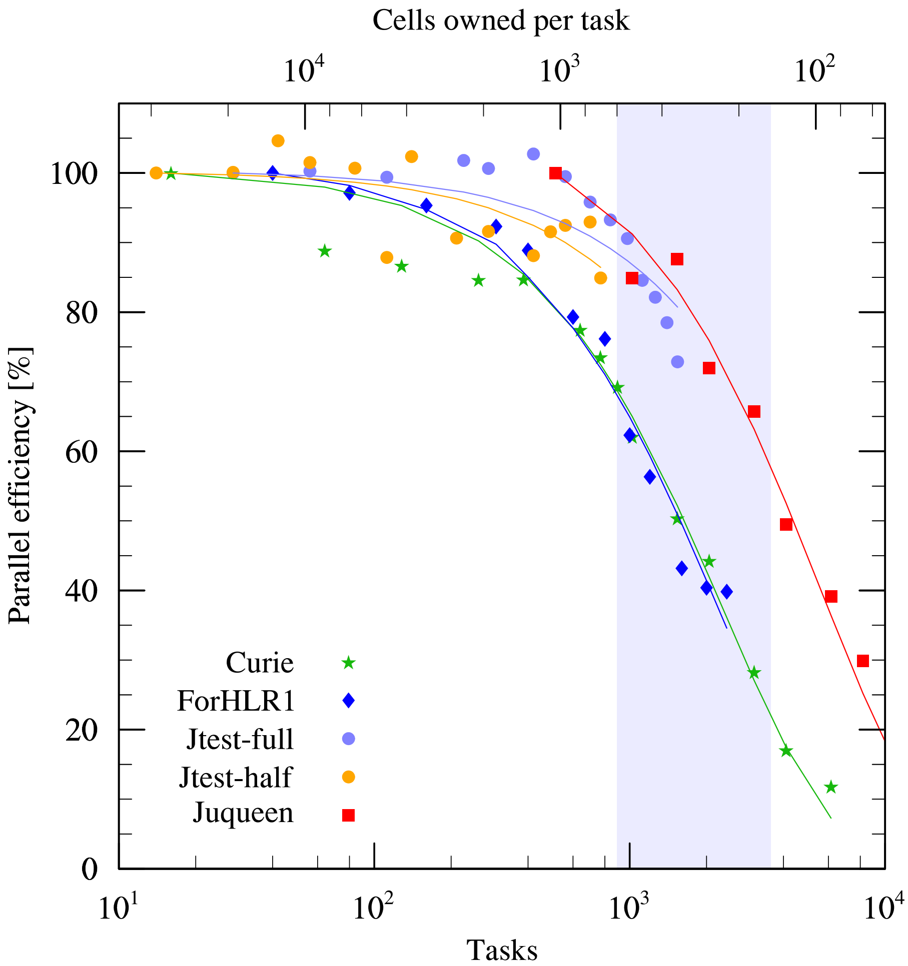

Figure 11. Scaling of the 60–12 km variable mesh test case.

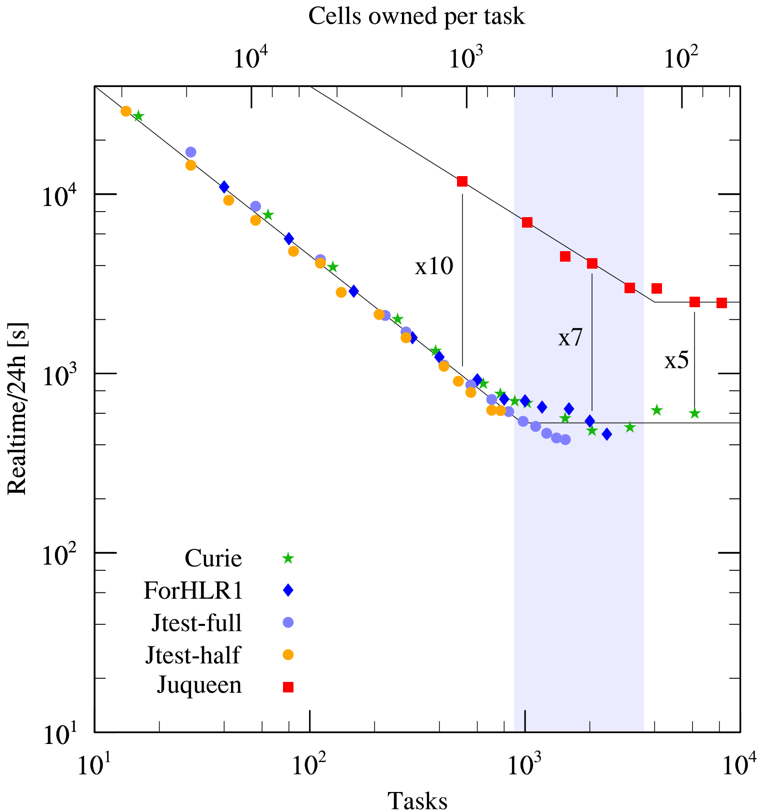

Figure 12. Total runtimes [s] for the variable 60–12 km mesh with 535 554 grid cells, indicated are time ratios between the Linux-cluster systems Curie, ForHLR1 and Juropatest, and the Bluegene system Juqueen.

GMDD
8, 6987–7061, 2015

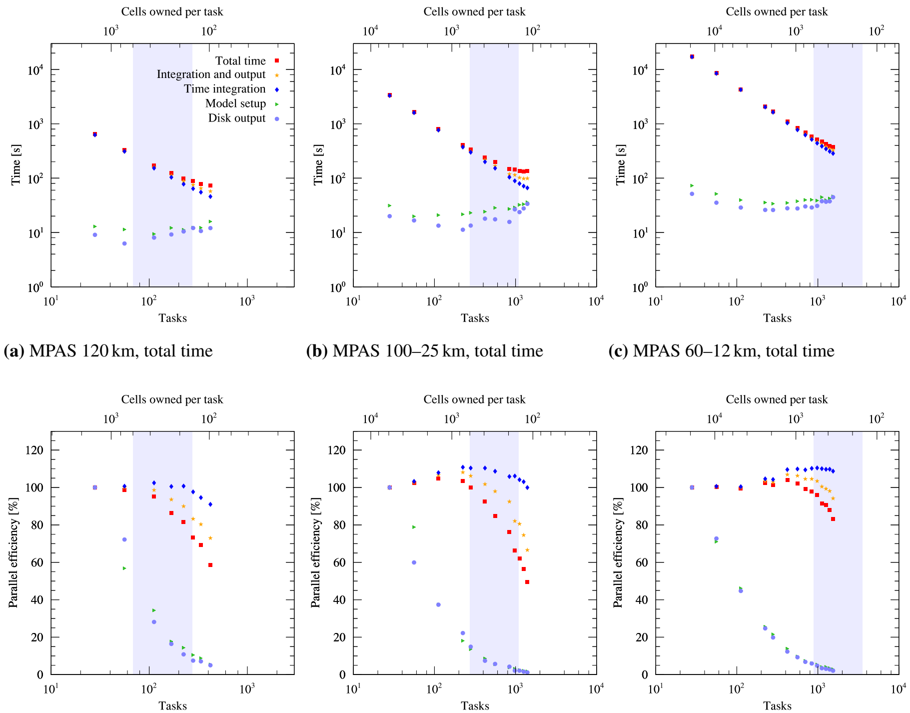

(a) MPAS 120 km, total time **(b)** MPAS 100–25 km, total time **(c)** MPAS 60–12 km, total time

(d) MPAS 120 km, parallel efficiency **(e)** MPAS 100–25 km, parallel efficiency **(f)** MPAS 60–12 km, parallel efficiency

Figure 13. (a–c) Required time for a 24 h integration [s] and **(d–f)** parallel efficiency [%] separated into time integration, model setup and disk output for the three test cases on Jtest-full. Also displayed are the total time/efficiency and a combination of time integration and disk output to reflect the parallel performance of MPAS-A for longer model runs, for which the initial setup costs are amortised.

GMDD
8, 6987–7061, 2015

Title Page
Abstract Introduction
Conclusions References
Tables Figures
◀ ▶
◀ ▶
Back Close
Full Screen / Esc
Printer-friendly Version
Interactive Discussion

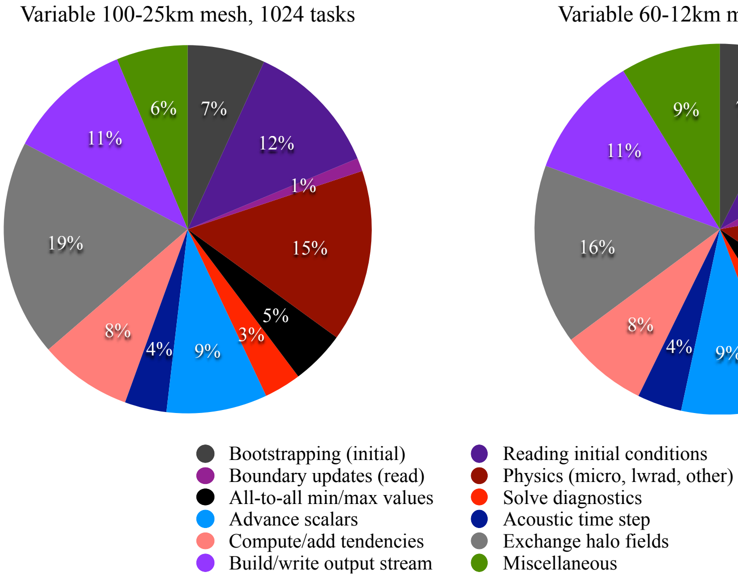

Figure 14. Scalasca/Score-P profiles for two selected runs on Juqueen to investigate the limitations for the breakdown of the parallel efficiency: (left) 1024-task run on the variable 100–25 km mesh with 163 842 grid cells; (right) 2048-task run on the variable 60–12 km mesh with 535 554 grid cells.

GMDD
8, 6987–7061, 2015

GMDD
8, 6987–7061, 2015

MPAS: an extreme scaling experiment

D. Heinzeller et al.

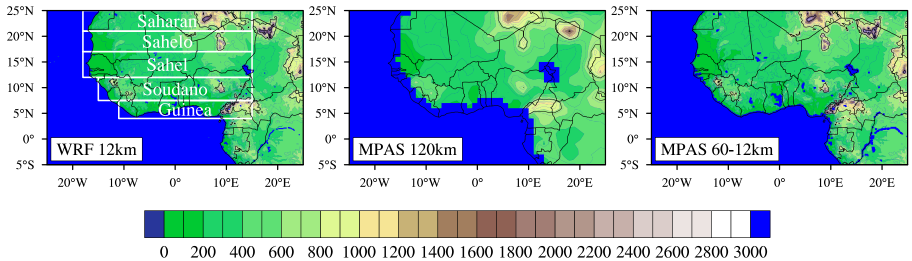

Figure 15. Model topography (terrain height in m) for the WRF reference and the two MPAS model runs for the West African WRF domain. The left panel also indicates five distinct agro-climatical zones, following a gradient of decreasing annual precipitation from South to North.

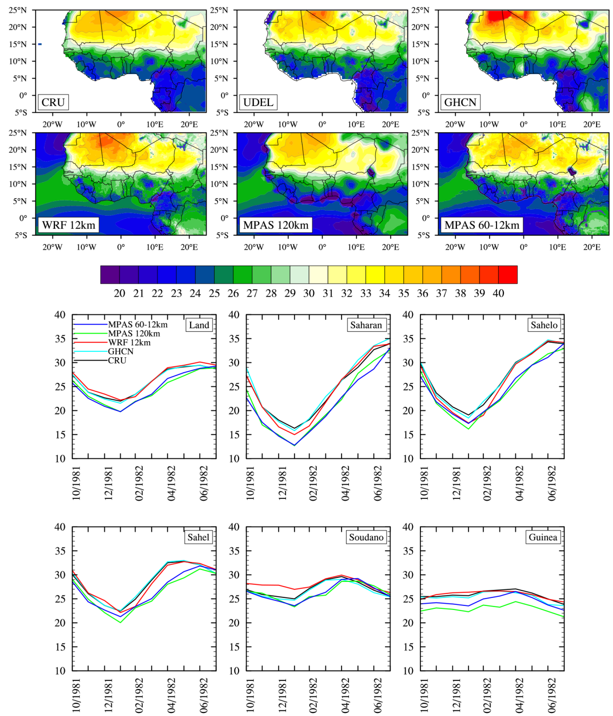

Figure 16. (top) Mean near-surface temperature (over land) in °C for July 1982 for the three observational data sets CRU, UDEL, GHCN, the WRF reference and the two MPAS model runs; (bottom) annual cycle of mean near-surface temperature over the entire land area and the five agro-climatical zones depicted in Fig. 15.

GMDD
8, 6987–7061, 2015

MPAS: an extreme scaling experiment

D. Heinzeller et al.

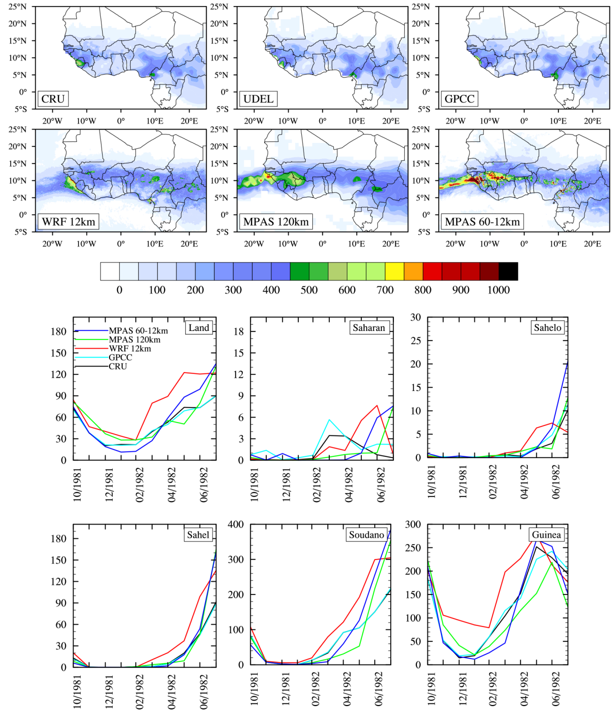

Figure 17. (top) Monthly precipitation (over land) in mm for July 1982 for the three observational data sets CRU, UDEL, GPCC, the WRF reference and the two MPAS model runs; (bottom) annual cycle of monthly precipitation over the entire land area and the five agro-climatical zones depicted in Fig. 15.

GMDD
8, 6987–7061, 2015
MPAS: an extreme scaling experiment
D. Heinzeller et al.

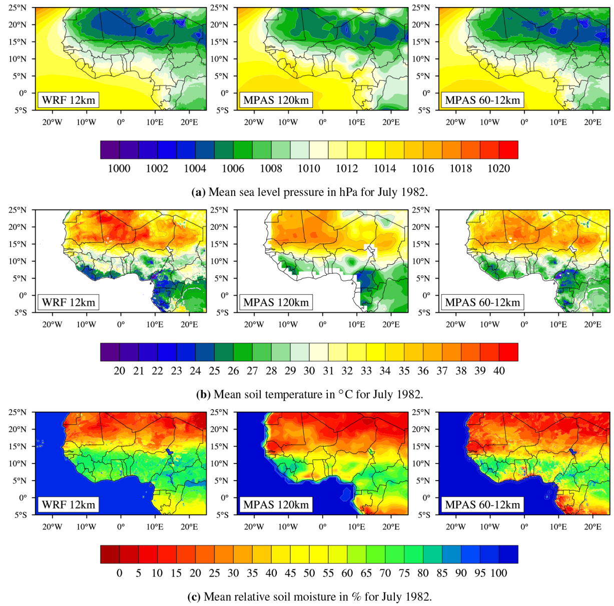

Figure 18. (a) Mean sea level pressure, **(b)** mean soil temperature, and **(c)** mean relative soil moisture over land for July 1982 for the WRF reference and the MPAS model runs.

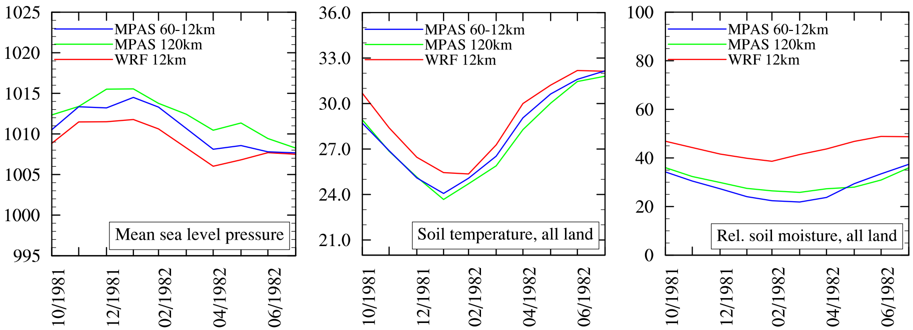

Figure 19. Annual cycle of (left) mean sea level pressure in hPa, (middle) mean soil temperature in °C, and (right) mean relative soil moisture in % over land for the WRF reference and the MPAS model runs.

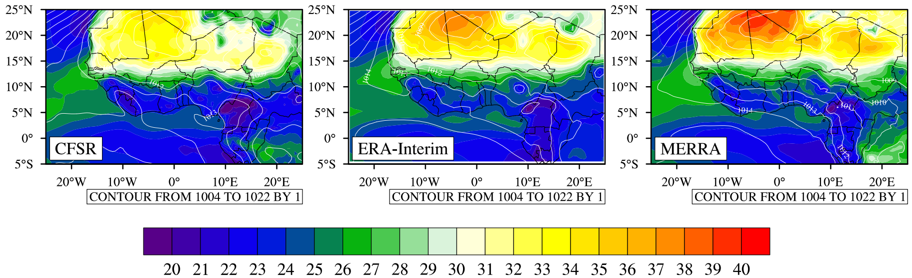

Figure 20. Mean near-surface temperature in °C for July 1982 for the three re-analyses CFSR, ERA-Interim and MERRA. Overlaid in white are contour lines of the mean sea level pressure in hPa in steps of 1 hPa.

GMDD
8, 6987–7061, 2015

Title Page
Abstract Introduction
Conclusions References
Tables Figures
◀ ▶
◀ ▶
Back Close
Full Screen / Esc
Printer-friendly Version
Interactive Discussion

GMDD
8, 6987–7061, 2015

MPAS: an extreme scaling experiment

D. Heinzeller et al.

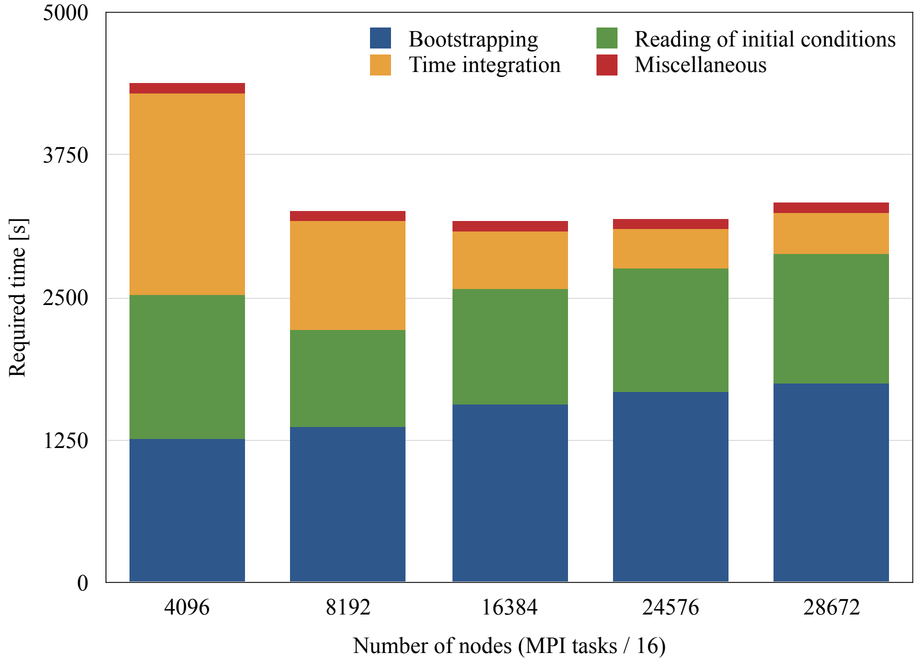

Figure 21. Required times for individual steps of the 3 km test runs on Juqueen (18 s time step).